Analysis of Thermoelastic Waves in a Two-Dimensional Functionally Graded Materials Domain by the Meshless Local Petrov-Galerkin (MLPG) Method

Ahmad Akbari R.[1], Akbar Bagri[2], Stéphane P. A. Bordas[3,4]
Timon Rabczuk[5]

Abstract: This contribution focuses on the simulation of two-dimensional elastic wave propagation in functionally graded solids and structures. Gradient volume fractions of the constituent materials are assumed to obey the power law function of position in only one direction and the effective mechanical properties of the material are determined by the Mori–Tanaka scheme. The investigations are carried out by extending a meshless method known as the Meshless Local Petrov-Galerkin (MLPG) method which is a truly meshless approach to thermo-elastic wave propagation. Simulations are carried out for rectangular domains under transient thermal loading. To investigate the effect of material composition on the dynamic response of functionally graded materials, a metal/ceramic (Aluminum (Al) and Alumina (Al_2O_3) are considered as ceramic and metal constituents) composite is considered for which the transient thermal field, dynamic displacement and stress fields are reported for different material distributions.

Keywords: Thermoelasticity, wave propagation, Functionally graded materials, MLPG.

1 Introduction

Functionally graded materials (FGM) are now ubiquitous in structures arising in mechanical and aerospace engineering. These materials are endowed with gradually varying material properties (structural, thermal, etc.) in one or more directions. If properly designed, these functionally graded materials inherit the advantages of

[1] Department of Energy, Power and Water Institute of Technology, Tehran, Iran
[2] Division of Engineering, Brown University, Providence, RI 02912, USA
[3] Royal Academy of Engineering/Leverhulme Senior Research Fellow
[4] Corresponding author stephane.bordas@alumni.northwestern.edu
[5] Institute of Structural Mechanics, Bauhaus-University Weimar Marienstraße 15, 99423 Weimar, Germany

their constituents making them ideal as, e.g. thermal barrier coatings. In order to design and optimize these materials, it is crucial to understand and predict their behavior, which often includes tackling coupled physical actions such as thermo-, electrico, hydro- and chemico-mechanical actions. Because of the complexity of both the materials and the loading conditions, it is usually not possible to obtain analytical results, and recourse to numerical methods is a generality.

This paper focuses on one such particular combination of external actions where an elastic wave propagates through a functionally graded material. To fix ideas, an aluminum ceramic composite is studied here. Numerical methods are numerous, the most widely used of which is the finite element method (FEM) and meshfree methods (MMs). The latter class of methods provides higher order continuity for the solution, facilitates the treatment of moving interfaces, and makes adapting the computational grid to the solution straightforward compared to the FEM. However, these methods are usually computationally costly and require special care for numerical integration as well as the enforcement of boundary conditions. The interested reader is referred to the recent review [Nguyen, V P; Rabczuk, T; Bordas, S; Duflot, M. (2008)], where an open-source MATLAB toolbox is also provided. Partition of unity enrichment [Melenk, J.M. and Babuska, I. (1996)] provides the FEM with the capability to be adapted to the solution sought through the incorporation of special functions within the approximation space. The extended and generalized finite element method (XFEM/GFEM) [Belytschko, T and Black, T. (1999)] are examples of partition of unity enriched finite element methods, which have been applied to a wide range of fields and may have the capacity to bridge the gap between FEM and MMs. The interested reader is referred to [Karihaloo, B L and Xiao, Q Z. (2003)] for a review, and [Bordas, Stephane P.A.; Nguyen, P V; Dunant, C; Dang, H N; Guidoum, A, (2006)] for an open source C++ XFEM library.

The long-term goal of this research is to assess the failure of functionally graded materials in electro-mechanical settings, for which we believe that meshfree methods have distinct advantages [Rabczuk, T; Bordas, S and Zi, G. (2007)], Bordas, S, Rabczuk, T and Zi, G. (2008)] and Rabczuk, T; Bordas, S; Nguyen, P V; Zi, G, (2008)].

Research into meshless methods is very active. After the work of [Nayroles, B, Touzot, G and Villon, P. (1992)], who proposed a diffuse element method which only used a mesh of nodes and a boundary description to develop the Galerkin equations, several meshless methods have spurred the interest of researchers, such as the element-free Galerkin method (EFG) [Belytschko, T, Lu, Y Y and Gu, L. (1994)], hp-clouds [Duarte, C A and Oden, J T. (1996)], the reproducing kernel particle method (RKPM) [Liu, W K, et al. (1996)], and, finally, the meshless lo-

cal Petrov-Galerkin method [Atluri, S N and Zhu, T. (1998)]. The meshless local Petrov-Galerkin method compared to the other meshless methods is a "truly meshless" approach, as it does not need elements or meshes, either for interpolation purposes, or for integration purposes. Two truly meshless methods, the meshless local Petrov-Galerkin (MLPG) method and the meshless local boundary integral equation (LBIE) method, have been developed by [Atluri, S N and Zhu, T. (1998)] and [Atluri, S N, Kim, H G and Cho, J Y. (1999)] for solving linear and non-linear boundary problems. Both of these methods are truly meshless, as no finite element/or boundary element meshes are required in these two approaches, neither for purposes of approximation of the trial and test functions for the solution variables, nor for the purpose of integration of the weak-form (either symmetric or unsymmetric).

Functionally graded materials (FGMs) are new branch of materials which may combine the desired properties of materials to enhance the capability of the structures to withstand various mechanical and thermal loads. The material properties of FGMs change gradually with position. Since the material properties of FGMs vary smoothly, these materials provide macroscopic properties that are complementary to now conventional composite materials in which microscopic properties change abruptly across the interface between layers, fiber/matrix and can result in large interfacial stresses and consequential delamination.

This delamination phenomenon is much more critical when abruptly varying thermal loads are applied to the composite structure. The applicability of FGMs in various areas of engineering has incited their detailed study. As briefly mentioned above, FGMs may be used as thermal barriers where a material with lower thermal conductivity is incorporated within the main structural material in order to help withstand thermal loads [Hasselman, D P.H and Youngblood, G E. (1978)].

Analyses of thermal stresses in FG elastic structures show that FGMs can indeed reduce the thermal stresses, e.g. see [Noda, N and Tsuji, T (1990)]. [Reddy, J N, Wang, C M and Kitipornchai, S. (1999)] studied the axisymmetric bending and stretching of FG solids and annular circular plates using the first-order shear deformation Mindlin plate theory. An analytical solution for functionally graded thick spheres under combined steady mechanical and thermal loads is presented by [Eslami, M R, Babai, M H and Poultangari, R. (2005)]. In their work, these authors provided a closed form solution of the problem where a simple power law function is considered for the material properties' distributions. [Shakeri, M, Akhlaghi, M and Hoseini, S M. (2006)] presented the analysis of layered FG thick hollow cylinders under a dynamic load where the functional grading is simulated by assuming the cylinder to be made of a succession of cylindrical isotropic layers.

[Chi, L F and Chung, Y L. (2006)] derived analytical solutions for FG plates un-

der transverse loads in the form of a Fourier series expansion. They studied elastic, rectangular, and simply supported FGM plates of medium thickness and confirmed their results through finite element analysis. [Zhang, G M and Batra, R C. (2007)] studied the wave propagation, under uniaxial strain conditions, in an FG plate where the material properties vary continuously in the direction of wave propagation. [Qian, L F and Batra, R C. (2005)] analyzed the transient heat conduction in a functionally graded thick plate by using a higher-order plate theory and a meshless local Petrov-Galerkin (MLPG) method. In [Qian, L F and Batra, R C. (2004)], the same authors considered the MLPG method for investigation of the transient thermoelastic deformations of a thick functionally graded plate with edges held at a uniform temperature. [Sladek, J, Sladek, V and Hon, Y C. (2006)] used the same MLPG method to solve stationary and transient heat conduction inverse problems in two-dimensional (2D) and three-dimensional (3D) axisymmetric bodies. [Ching, H K and Yen, S C. (2005)] presented MLPG formulations and solutions to the general thermo-mechanical problem of a 2D FG solid. They first considered the case of an FG link bar, then a pressurized hollow cylinder is. The most general problem these authors solved in their contribution is the thermoelastic analysis of cylindrical bending, for a two-phase FG material.

Sladek and et al applied MLPG method for 3-D problems such as orthotropic shallow shells under a thermal load [Sladek J, Sladek, V; Solek, P; Wen, P H; Atluri, S N. (2008)], solution of steady-state and transient heat conduction problems in a continuously nonhomogeneous anisotropic medium with randomly distributed nodal points [Sladek, J; Sladek, V; Tan, C L; Atluri, S N. (2008)], solution of static and elastodynamic problems [Sladek J, Sladek V, Solek P. (2009)]. MLPG method for transient linear thermoelastic analysis is presented by [Sladek, J; Sladek, V;Solek, P;Tan, C L; Zhang, Ch. (2009)]. A meshless method based on the local Petrov-Galerkin approach is proposed by [Sladek, J; Sladek, V; Zhang, Ch; Solek, P. (2007)] for the solution of boundary value problems for coupled thermo-electro-mechanical fields. They used the Heaviside step function as test functions in the local integral equations to the derivation of the local boundary-domain integral equations and the Laplace transform technique to eliminate time dependence in their equations [Sladek J, Sladek, V; Solek, P; Wen, P H; Atluri, S N. (2008) ;Sladek, J; Sladek, V; Zhang, Ch; Solek, P. (2007)].

MLPG method is proposed to solve the interface crack problem between two dissimilar anisotropic elastic solids [Sladek, J; Sladek, V; Wünsch, M; Zhang, Ch. (2009)]. Meshless local Petrov-Galerkin collocation method is applied to compute two dimensional heat conduction problems in irregular domain [XueHong, WU; ShengPing, SHEN; WenQuan, TAO. (2007)]. [Heaney, C; Augarde, C; Deeks, A. (2010)] extended a novel numerical method, based on the Meshless Local Petrov-

Galerkin (MLPG) method, to the modelling of elasto-plastic materials. Their extended method is particularly suitable for problems in geomechanics, as it permits inclusion of infinite boundaries.

Numerical solutions obtained by the MLPG method are presented for static deformations, free and forced vibrations of an FG cantilever beam by [Qian, L F and Ching, H K. (2004)]. These authors reported results for the static, free and forced vibration analyses of an FG cantilever beam. [Eslami, M R; Akbari R., A; Bagri, A; Tajdari, M. (2007)] presented a meshless method based on the local Petrov–Galerkin approach for the static analysis of thermal stresses in a two-dimensional domain made of isotropic linear thermoelastic functionally graded materials. [Berezovski, A, Engelbrecht, J and Maugin, G A. (2003)] numerically studied the propagation of stress waves in functionally graded materials by means of the composite wave-propagation algorithm. Two distinct models of FGMs were considered: (i) a multilayered metal–ceramic composite with averaged properties within layers; (ii) randomly embedded ceramic particles in a metal matrix with prescribed volume fraction. The simulations demonstrate the applicability of that algorithm to the modelling of FGMs without any averaging procedure. These simulations show the influence of the material models on the characteristics of the stress wave when the FG structure is subjected to impact loading.

[Liu, G R, Han, X and Lam, K Y. (1999)] proposed a method to investigate elastic waves in functionally graded plates excited by plane pressure wavelets, where the FGM plate is divided into linearly inhomogeneous elements (LIEs). These authors have derived a general solution for the equations of motion governing the LIE. The general solution was then used together with the boundary and continuity conditions to obtain the displacement and stress in the frequency domain for an arbitrary FGM plate. Relationships between the surface displacement response and the material mechanical properties of FGM plates were also obtained which may be used for the characterization of FGM plate materials. [Han, X; Liu, G R; Xi, Z C; Lam, K Y. (2001)] have presented a hybrid method, which combines finite element method with the Fourier transformation method for analyzing transient wave in a cylinder made of functionally graded material.

In the present paper, we propose a new numerical method for the simulation of elastic wave propagation in isotropic linear elastic functionally graded materials. We then validate this numerical technique and employ it to shed light on the behavior of functionally graded materials in a two-dimensional setting. Our contribution is therefore two-fold

1) propose and validate an accurate numerical scheme to study the dynamic response of a two-dimensional functionally graded domain under thermal loads;

2) help the understanding of the behavior of functionally graded materials under thermal loads.

The method we propose relies on the meshless local Petrov–Galerkin (MLPG) method, a "truly-meshless" method that was briefly introduced above and will be further explained in Section 2. The material properties of the domain are assumed to change continuously and be position dependent functions. Here, we use a power law form function to describe the volume fraction change and the elastic material properties are calculated using the Mori-Tanaka scheme [Mori, T and Tanaka, K. (1973)].

As will be made clear below, the MLPG method does not require a mesh, neither for numerical integration nor for the construction of the approximation. In this work, we use a regular array of nodes (sometimes also called particles) and construct the approximation functions using the moving least squares (MLS) method Belytschko, T, Lu, Y Y and Gu, L. (1994)]. The MLS approximation technique is now well-known, and its basic ingredients are recalled for completeness in Section 2.1.

The MLPG is employed in Section 2.2. and Section 2.3, to obtain a discretized local weak form for the energy balance equation and the dynamic thermo-elasticity equations in a two-dimensional functionally-graded domain, respectively. As described in the recent meshfree review [Nguyen, V P; Rabczuk, T; Bordas, S; Duflot, M. (2008)], the essential boundary conditions in the MLPG approach are enforced by the matrix transformation technique [Qian, L F and Batra, R C. (2004)].

Section 3 then describes how the effective properties of the functionally graded materials considered are calculated before briefly describing, in Section 4, the time integration scheme.

The MLPG formulation proposed is first validated, in Section 5.1., in the case of an isotropic, homogeneous material. In Section 5.2., the thermal stress calculation is then validated, before, in Section 5.3., analyzing in-depth the problem of thermo-elastic wave propagation in a two-dimensional functionally graded material. In particular, the effects of material composition on temperature, displacement and stress distribution and its influence on the wave propagation speed are studied in detail.

Section 6. concludes the paper with a discussion and outlook onto future work.

2 Meshless local Petrov-Galerkin (MLPG) method and thermo-elastic wave propagation problem formulation

2.1 *Moving least square (MLS) approximation technique*

A simple and effective scheme to approximate scattered data is the moving least square (MLS) method [Belytschko, T, Lu, Y Y and Gu, L. (1994)]. In this section, a brief summary of this technique is given. As the MLS has been used extensively in the meshfree (meshless) literature, only the most salient features are provided here, and the interested reader is referred back to the recent review paper on mesh-free methods [Nguyen, V P; Rabczuk, T; Bordas, S; Duflot, M. (2008)] where a MATLAB code for MLS approximations and their enrichment is provided.

Consider Ω_x, a neighborhood of $\mathbf{x}$ which is denoted as the domain of definition of the MLS approximation at $\mathbf{x}$, and is located in the problem domain Ω. To approximate the distribution of function $\psi(\mathbf{x},t)$ in Ω_x over a number of randomly located nodes $\{\mathbf{x}_I\}$, $I = 1,2,\cdots,N_d$, the moving least squares approximant $\psi^h(\mathbf{x},t)$ of ψ, $\forall \mathbf{x} \in \Omega_x$ can be defined, for all times, by

$$\psi^h(\mathbf{x},t) = \mathbf{p}^T(\mathbf{x})\,\mathbf{a}(\mathbf{x},t),\, \forall \mathbf{x} \in \Omega_x \tag{1}$$

where $\mathbf{p}^T(\mathbf{x}) = [p_1(\mathbf{x})\ p_2(\mathbf{x})\ldots p_m(\mathbf{x})]$ is a complete monomial basis, $\mathbf{p}^T(\mathbf{x}) = \begin{bmatrix}1\ x\ y\ x^2\ xy\ y^2\end{bmatrix}$ is the number of terms in the basis, and $\mathbf{a}(\mathbf{x},t)$ is a vector containing the coefficients $a_j(\mathbf{x},t)$, $j = 1, 2, \ldots, m$, which are functions of the space coordinates $\mathbf{x}$, and term t is the time variable.

Remark In the present research, we use the quadratic polynomial basis $\mathbf{p}^T(\mathbf{x}) = \begin{bmatrix}1\ x\ y\ x^2\ xy\ y^2\end{bmatrix}$ for 2-D.

The coefficient vector $\mathbf{a}(\mathbf{x},t)$ is determined by minimizing a weighted discrete L2 norm, which is defined as

$$J(\mathbf{a}(\mathbf{x},t)) = \sum_{I=1}^{N_d} w_I(\mathbf{x}) \left[\mathbf{p}^T(\mathbf{x}_I)\,\mathbf{a}(\mathbf{x},t) - \hat{\psi}_I(t) \right]^2 \tag{2}$$

where $w_I(\mathbf{x})$ is a weight function associated with node I, with $w_I(\mathbf{x}) > 0$ for all $\mathbf{x}$ in the support of $w_I(\mathbf{x})$, $\mathbf{x}_I$ denotes the position vector of node I, N_d is the number of nodes in Ω_x for which the weight functions $w_I(\mathbf{x}) > 0$.

Remark It should be noted that $\hat{\psi}_I$ are the fictitious nodal values, and not the actual nodal values of the trial function $\psi^h(\mathbf{x},t)$, in general (cf. second line in Eq. 3). This is because the functions ϕ_I are not interpolants, but only approximants, i.e. the approximation does not pass through the data points. This is also known as the lack of Kronecker-Delta property and leads to difficulties in imposing essential boundary conditions in MLS-based meshfree methods. Details on this are provided in the

following papers, among others: [Huerta, A; Belytschko, T; Fernandez-Mendez, S; Rabczuk, T. (2004)] and [Nguyen, V P; Rabczuk, T; Bordas, S; Duflot, M. (2008)].

After some algebraic manipulations and substituting for the vector $\mathbf{a}(\mathbf{x},t)$ in Eq.1, the following relation may be obtained

$$\psi^h(\mathbf{x},t) = \sum_{I=1}^{N_d} \phi_I(\mathbf{x})\,\hat{\psi}_I(t) = \mathbf{\Phi}^T(\mathbf{x})\hat{\mathbf{\Psi}}(t),$$

$$\psi^h(\mathbf{x},t) = \psi_I \neq \hat{\psi}_I(t), \mathbf{x} \in \Omega_x \tag{3}$$

in which

$$\hat{\mathbf{\Psi}}(t) = [\hat{\psi}_1(t) \ \hat{\psi}_2(t) \ \dots \ \hat{\psi}_{N_d}(t)]^T$$

$$\mathbf{\Phi}^T(\mathbf{x}) = [\phi_1(\mathbf{x}) \ \phi_2(\mathbf{x}) \ \dots \ \phi_{N_d}(\mathbf{x})] = \mathbf{p}^T(\mathbf{x})\,\mathbf{A}^{-1}(\mathbf{x})\,\mathbf{B}(\mathbf{x}) \tag{4}$$

Where the matrices $\mathbf{A}(\mathbf{x})$ and $\mathbf{B}(\mathbf{x})$ are defined by

$$\mathbf{A}(\mathbf{x}) = \sum_{I=1}^{N_d} w_I(\mathbf{x})\,\mathbf{p}(\mathbf{x}_I)\,\mathbf{p}^T(\mathbf{x}_I) \tag{5}$$

$$\mathbf{B}(\mathbf{x}) = [w_1(\mathbf{x})\,\mathbf{p}(\mathbf{x}_1) \ w_2(\mathbf{x})\,\mathbf{p}(\mathbf{x}_2) \ \cdots \ w_{N_d}(\mathbf{x})\,\mathbf{p}(\mathbf{x}_{N_d})] \tag{6}$$

Here N_d is the number of nodes in the neighborhood of $\mathbf{x}$ for which the weight function $w_I(\mathbf{x})$ has a nonzero value. A spline-type weight function, with a rectangular support, is chosen in this work:

$$w_I(\mathbf{x},\mathbf{x}_I) = w_I^x(x,x_I) \times w_I^y(y,y_I) \tag{7}$$

where $w_I^x(x,x_I)$, $w_I^y(y,y_I)$ are the 1-D quartic spline functions in the x and y directions, respectively, and are defined as

$$w_I^x(x,x_I) = \begin{cases} 1 - 6\left(\frac{d_I^x}{r_I^x}\right)^2 + 8\left(\frac{d_I^x}{r_I^x}\right)^3 - 3\left(\frac{d_I^x}{r_I^x}\right)^4 & 0 \leq d_I^x \leq r_I^x \\ 0 & d_I^x \geq r_I^x \end{cases} \tag{8}$$

$$w_I^y(y,y_I) = \begin{cases} 1 - 6\left(\frac{d_I^y}{r_I^y}\right)^2 + 8\left(\frac{d_I^y}{r_I^y}\right)^3 - 3\left(\frac{d_I^y}{r_I^y}\right)^4 & 0 \leq d_I^y \leq r_I^y \\ 0 & d_I^y \geq r_I^y \end{cases} \tag{9}$$

where $d_I^x = |x - x_I|$, $d_I^y = |y - y_I|$ are the distances from node I located at $\mathbf{x}_I = \{x_I, y_I\}^T$ to point at $\mathbf{x} = \{x, y\}^T$ and r_I^x, r_I^y are the size of support of the weight functions w_I^x, w_I^y associated with node I in the x and y directions, respectively.

It can be easily seen in Fig. 1 that the spline weight functions given by Eqs. 9 and 10 possess C^1 continuity. It can also be shown that the regularity of the weight

function is inherited by the shape functions. The resulting approximation, employed throughout this paper, relies on the quadratic basis $\mathbf{p}(\mathbf{x})$, and the 4th-order spline weight function, thus, the approximation is:

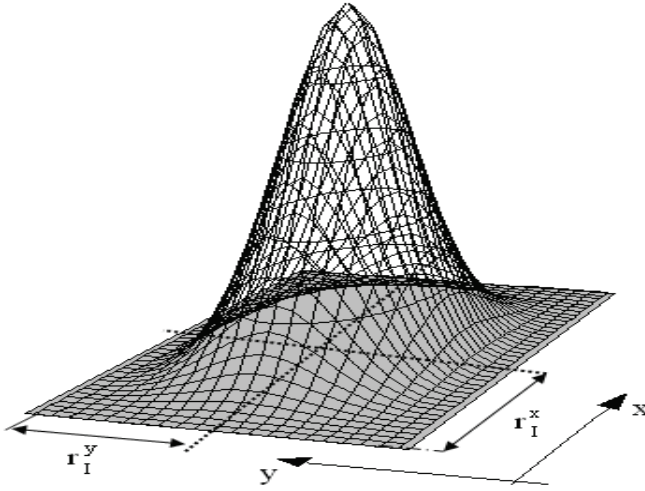- C^1 continuous over the entire domain;

- Second order complete.

Figure 1: Quartic spline weight function with a rectangular support, used in the MLS approximation.

2.2 MLPG formulation of energy balance equation in a 2-D domain

A 2-D solid domain, Ω, made of isotropic linear thermo-elastic functionally graded material is considered. It is bounded by Γ in a rectangular Cartesian coordinate system ($\Omega = [0, l_x] \times [0, l_y]$). In the absence of sources of internal energy, the energy balance of domain Ω writes

$$
\begin{aligned}
\nabla \cdot (k \nabla T) &= \rho c \frac{\partial T}{\partial t} && \text{in } \Omega \times [0, t] \\
T &= \tilde{T}(\mathbf{x}, t) && \text{on } \Gamma_T \times [0, t] \\
-k \nabla T &= \tilde{\mathbf{q}}(\mathbf{x}, t) && \text{on } \Gamma_q \times [0, t] \\
T(\mathbf{x}, 0) &= T_0 && \text{in } \Omega
\end{aligned}
\tag{10}
$$

where T is the absolute temperature, ρ is the mass density, k is the heat conductivity coefficient, c is the specific heat, t is the time variable and $\mathbf{x} = x\hat{\mathbf{e}}_x + y\hat{\mathbf{e}}_y$ is the space coordinate vector. The initial temperature of the domain is assumed to be T_0 and the thermal boundary conditions may be defined as a prescribed temperature $\tilde{T}$ on Γ_T and given heat flux $\tilde{\mathbf{q}}$ on Γ_q. In the preceding equations, ∇ is the vector gradient operator defined by $\nabla = \frac{\partial}{\partial x}\hat{\mathbf{e}}_x + \frac{\partial}{\partial y}\hat{\mathbf{e}}_y$, in which $\hat{\mathbf{e}}_x$ and $\hat{\mathbf{e}}_y$ are the unit vectors in the x and y directions of the coordinate system, respectively. It is more convenient to introduce the above equations in dimensionless form:

$$\bar{x} = \frac{x}{l}, \quad \bar{t} = \frac{C_1^2}{\kappa_m}t, \quad \bar{y} = \frac{y}{l},$$
$$\bar{T} = \frac{T - T_0}{T_{ref}}, \quad \bar{\mathbf{q}} = \frac{l}{k_m T_{ref}}\mathbf{q} \tag{11}$$

in which

$$C_1 = \sqrt{(\lambda_c + 2\mu_c)/\rho_c}, \quad \kappa_m = \frac{k_m}{\rho_m c_m}, l = \kappa_m/C_1 \tag{12}$$

where subscripts c and m are used to indicate ceramic and metal properties, respectively and the overbar indicates dimensionless parameters. In the previous equations, κ is the thermal diffusivity, C_1 is the purely elastic dilatational wave speed in the ceramic material, l is a standard length, and T_{ref} is a reference temperature. By using the dimensionless terms defined by Eqs. 11 and 12, Eq. 10 become (the overbar is dropped for simplicity)

$$
\begin{aligned}
\frac{1}{k_m}\nabla.(k\nabla T) &= \frac{\rho c}{\rho_m c_m}\frac{\partial T}{\partial t} \quad &\text{in } \Omega \times [0,t] \\
T &= \tilde{T}(\mathbf{x},t) \quad &\text{on } \Gamma_T \times [0,t] \\
-\frac{k}{k_m}\nabla T &= \tilde{\mathbf{q}}(\mathbf{x},t) \quad &\text{on } \Gamma_q \times [0,t] \\
T(\mathbf{x},0) &= 0 \quad &\text{in } \Omega
\end{aligned}
\tag{13}
$$

Instead of writing the global weak form of the governing equations, one version of the MLPG method constructs the weak form over local overlapping subdomains, which are here rectangles around each node as shown in Fig. 2. The interested reader is referred to [Atluri, S N and Zhu, T. (1998); Atluri, S N, (2004)] for more details on the formulation of the MLPG as well as [Fries, T P and Matthies, H G. (2003)]. The local symmetric weak form over the I-th local thermal subdomain, Ω_s^I, writes

$$\int_{\Omega_s^I} v_I \left(\frac{1}{k_m}\nabla.(k\nabla T) - \frac{\rho c}{\rho_m c_m}\frac{\partial T}{\partial t} \right) d\Omega = 0 \tag{14}$$
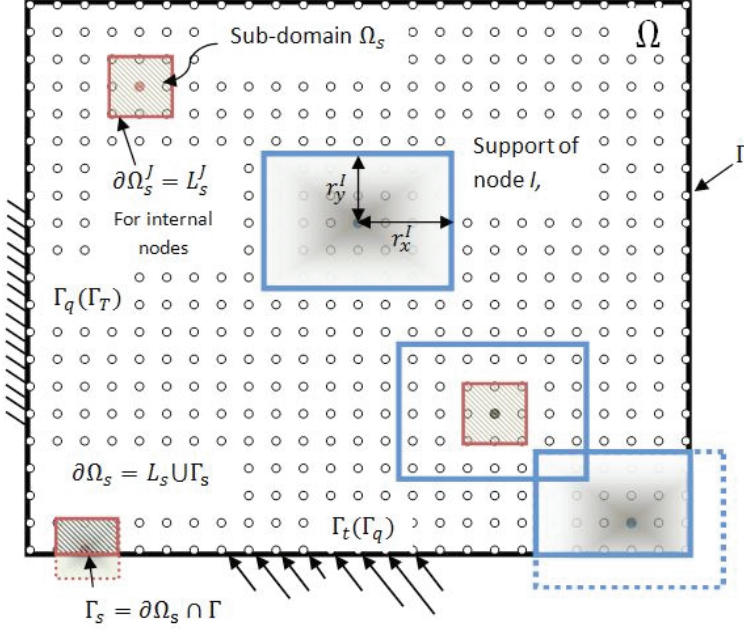
Figure 2: Meshless Local Petrov-Galerkin scheme for a two dimensional domain.

In the preceding equation, v_I is the test function. In the MLPG method used in the present work, the test function is chosen as the weight function used in the MLS approximation but with a different support size. The test function, v_I, associated with node I, is defined as

$$v_I(\mathbf{x}, \mathbf{x}_I) = v_I^x(x, x_I) \times v_I^y(y, y_I) \tag{15}$$

By using the relation $v_I \nabla.(k\nabla T) = \nabla.(v_I k \nabla T) - \nabla v_I . k \nabla T$ and applying the divergence theorem to Eq. 14 we obtain

$$\int_{\partial \Omega_s^I} v_I \frac{k}{k_m} \nabla T . \mathbf{n} \, d\Gamma - \int_{\Omega_s^I} \nabla v_I . \frac{k}{k_m} \nabla T \, d\Omega - \int_{\Omega_s^I} v_I \left(\frac{\rho c}{\rho_m c_m} \frac{\partial T}{\partial t} \right) d\Omega = 0 \tag{16}$$

in which $\mathbf{n} = n_x \hat{\mathbf{e}}_x + n_y \hat{\mathbf{e}}_y$ is the unit outward normal vector to the local subdomain boundary $\partial \Omega_s^I$, see Fig. 2. Herein, the boundary $\partial \Omega_s^I$ of the I-th local subdomain consists of three parts, $\partial \Omega_s^I = L_s^I \cup \Gamma_{sT}^I \cup \Gamma_{sq}^I$ where L_s^I is the part of the local boundary that is entirely inside the global domain, Γ_{sq}^I is the part of the local boundary that coincides with the global heat flux boundary, i.e. $\Gamma_{sq}^I = \Gamma_q \cap \partial \Omega_s^I$ and Γ_{sT}^I is the part of the local boundary $\partial \Omega_s^I$ which coincides with the global temperature

boundary Γ_T, i.e. $\Gamma_{sT}^I = \Gamma_T \cap \partial \Omega_s^I$. Note that the test function will be zero on the part of the local subdomain boundary which is entirely inside the global domain. Thus, rearranging the unknown terms on the left side of Eq.16 gives

$$-\int_{\Gamma_{sT}^I} v_I \frac{k}{k_m} \nabla T . \mathbf{n} d\Gamma + \int_{\Omega_s^I} \nabla v_I . \frac{k}{k_m} \nabla T d\Omega$$

$$+ \int_{\Omega_s^I} v_I \frac{\rho c}{\rho_m c_m} \frac{\partial T}{\partial t} d\Omega = - \int_{\Gamma_{sq}^I} v_I \tilde{\mathbf{q}} . \mathbf{n} d\Gamma \quad (17)$$

Eq. 17 expresses the overall energy balance equation on subdomain Ω_s^I. By using Eq. 3 and substituting the temperature trial function $T^h(x,t)$ instead of the temperature variable, T, in Eq. 17, the discretized governing equations for the I-th local subdomain becomes

$$\mathbf{H}_I \hat{\mathbf{T}}(t) + \mathbf{R}_I \frac{d\hat{\mathbf{T}}(t)}{dt} = P_I(t) \ \text{ in } \Omega_s^I \times [0,t] \quad (18)$$

in which

$$\mathbf{H}_I = -\int_{L_{sT}^I} v_I \frac{k}{k_m} \mathbf{n} \mathbf{D}^{Th} \mathbf{\Phi}^{Th} d\Gamma + \int_{\Omega_s^I} \frac{k}{k_m} \mathbf{\varepsilon}_I^{Th} \mathbf{D}^{Th} \mathbf{\Phi}^{Th} d\Omega$$

$$\mathbf{R}_I = \int_{\Omega_s^I} v_I \frac{\rho c}{\rho_m c_m} \mathbf{\Phi}^{Th} d\Omega, \quad (19)$$

$$\hat{\mathbf{T}} = \begin{bmatrix} \hat{T}_1 & \hat{T}_2 & ... & \hat{T}_N \end{bmatrix}^T, \quad P_I = -\int_{\Gamma_{sq}^I} v_I \tilde{\mathbf{q}} . \mathbf{n} d\Gamma$$

where $\hat{T}_J$ (j=1,2, ..., N) is the fictitious value of the temperature at node j and N is the number of nodes that their weight functions have influence on subdomain I, i.e. $w_j(\mathbf{x}) > 0; \mathbf{x} \in \Omega_s^I$.

$$\mathbf{n} = \begin{bmatrix} n_x & n_y \end{bmatrix}, \quad \mathbf{\varepsilon}_I^{Th} = \begin{bmatrix} \partial v_I / \partial x & \partial v_I / \partial y \end{bmatrix},$$

$$\mathbf{D}^{Th} = \begin{bmatrix} \partial / \partial x & \partial / \partial y \end{bmatrix}^T, \quad \mathbf{\phi}^{Th} = \begin{bmatrix} \phi_1 & \phi_2 & ... & \phi_N \end{bmatrix} \quad (20)$$

Eq. 18 is a ordinary differential equation that states the energy balance on the *I*-th local subdomain. By writing the equations for all subdomains, we arrive at a set of coupled ordinary differential equations which represent the energy balance on the entire global domain and may be given in matrix form as

$$\bar{\mathbf{H}} \hat{\mathbf{T}}(t) + \bar{\mathbf{R}} \frac{d\hat{\mathbf{T}}(t)}{dt} = \bar{\mathbf{P}}(t) \quad \text{in } \Omega \times [0,t] \quad (21)$$

where

$$\bar{\mathbf{H}} = \begin{bmatrix} \bar{\mathbf{H}}_1 \\ \bar{\mathbf{H}}_2 \\ \vdots \\ \bar{\mathbf{H}}_{N_{tot}} \end{bmatrix}, \quad \bar{\mathbf{R}} = \begin{bmatrix} \bar{\mathbf{R}}_1 \\ \bar{\mathbf{R}}_2 \\ \vdots \\ \bar{\mathbf{R}}_{N_{tot}} \end{bmatrix}, \quad \bar{\mathbf{P}} = \begin{Bmatrix} P_1 \\ P_2 \\ \vdots \\ P_{N_{tot}} \end{Bmatrix} \tag{22}$$

where $\bar{\mathbf{H}}_I$ and $\bar{\mathbf{R}}_I$ are the assembled coefficients of ordinary differential equations that state the energy balance of the entire domain. Also, N_{tot} is the total nodes distributed through the entire global domain.

2.3 MLPG formulation of dynamic thermoelastic deformation of a 2-D domain

In the absence of body forces, the dynamic thermoelastic deformation of an isotropic domain is governed by

$$\begin{aligned}
\nabla . \boldsymbol{\sigma} &= \rho \frac{\partial^2 \mathbf{u}}{\partial t^2} && \text{in } \Omega \times [0,t] \\
\mathbf{u} &= \tilde{\mathbf{u}} && \text{on } \Gamma_u \times [0,t] \\
\boldsymbol{\sigma} . \mathbf{n} &= \tilde{\mathbf{t}} && \text{on } \Gamma_t \times [0,t] \\
\mathbf{u}(\mathbf{x},0) &= \mathbf{u}_0(\mathbf{x}) && \text{in } \Omega \\
\frac{\partial \mathbf{u}(\mathbf{x},0)}{\partial t} &= \frac{\partial \mathbf{u}_0(\mathbf{x})}{\partial t} && \text{in } \Omega
\end{aligned} \tag{23}$$

where $\boldsymbol{\sigma}$ is the Cauchy stress tensor, $\mathbf{u} = u_x \hat{\mathbf{e}}_x + u_y \hat{\mathbf{e}}_y$ is the displacement vector, $\mathbf{u}_0$ is the initial displacement vector, $\tilde{\mathbf{u}}$ is the prescribed displacement on Γ_u and $\tilde{\mathbf{t}}$ is the given traction force on Γ_t. Also, $\mathbf{n}$ is the unit outward normal vector to the domain boundary Γ_t. The preceding equations are complemented with the thermal stress-strain relations and the kinematical strain-displacement equations to set the system of equations of thermo-elasticity of the isotropic functionally graded domain. The constitutive relations and the strain-displacement relationship in two dimensional Cartesian coordinates are

$$\begin{Bmatrix} \sigma_{xx} \\ \sigma_{yy} \\ \sigma_{xy} \end{Bmatrix} = \begin{bmatrix} \bar{\lambda} + 2\mu & \bar{\lambda} & 0 \\ \bar{\lambda} & \bar{\lambda} + 2\mu & 0 \\ 0 & 0 & 2\mu \end{bmatrix} \left(\begin{Bmatrix} \varepsilon_{xx} \\ \varepsilon_{yy} \\ \varepsilon_{xy} \end{Bmatrix} - \begin{Bmatrix} \bar{\alpha} \\ \bar{\alpha} \\ 0 \end{Bmatrix} \theta \right) \tag{24}$$

Here, ε_{ij} are the components of the strain tensor $\boldsymbol{\varepsilon}$, $\theta = T - T_0$ is the temperature

change, u_i is the component of the displacement vector and

$$\bar{\lambda} = \begin{cases} \lambda & \text{plane strain} \\ \lambda \; \frac{2\mu}{\lambda+2\mu} & \text{plane stress} \end{cases}$$
$$\bar{\alpha} = \begin{cases} \alpha \; \frac{3\lambda+2\mu}{2\lambda+2\mu} & \text{plane strain} \\ \alpha & \text{plane stress} \end{cases} \tag{25}$$

in which α is the coefficient of linear thermal expansion, and λ and μ are Lamé constants.

Similarly to the energy balance equation, the system of Eqs. 23 and 24 may be introduced in dimensionless form for convenience. To do so, it is useful to define the following dimensionless terms, in addition to those of Eq. 11:

$$\bar{\boldsymbol{\varepsilon}} = \frac{(\lambda_c + 2\mu_c)}{\beta_c \, T_{ref}} \boldsymbol{\varepsilon}, \quad \bar{\boldsymbol{\sigma}} = \frac{\boldsymbol{\sigma}}{\beta_c \, T_{ref}}, \quad \bar{\mathbf{u}} = \frac{(\lambda_c + 2\mu_c) \, C_1}{\kappa_m \, \beta_c \, T_{ref}} \mathbf{u} \tag{26}$$

in which

$$\beta_c = \alpha_c \, (3\lambda_c + 2\mu_c) \tag{27}$$

Here, the material properties with subscript c refer to the ceramic material properties. With the help of dimensionless parameters and dropping the overbar for convenience, the governing equations and boundary conditions become

$$\begin{aligned}
\nabla . \boldsymbol{\sigma} &= \frac{\rho}{\rho_c} \frac{\partial^2 \mathbf{u}}{\partial t^2} & \text{in } \Omega \times [0, t] \\
\mathbf{u} &= \tilde{\mathbf{u}} & \text{on } \Gamma_u \times [0, t] \\
\boldsymbol{\sigma} . \mathbf{n} &= \tilde{\mathbf{t}} & \text{on } \Gamma_t \times [0, t] \\
\mathbf{u}(\mathbf{x}, 0) &= \mathbf{u}_0(\mathbf{x}) & \text{in } \Omega \\
\frac{\partial \mathbf{u}(\mathbf{x}, 0)}{\partial t} &= \frac{\partial \mathbf{u}_0(\mathbf{x})}{\partial t} & \text{in } \Omega
\end{aligned} \tag{28}$$

Also, Eq. 24 can be recast in terms of the dimensionless parameters as

$$\begin{Bmatrix} \sigma_{xx} \\ \sigma_{yy} \\ \sigma_{xy} \end{Bmatrix} = \begin{bmatrix} \bar{\lambda}+2\mu & \bar{\lambda} & 0 \\ \bar{\lambda} & \bar{\lambda}+2\mu & 0 \\ 0 & 0 & 2\mu \end{bmatrix} \left(\frac{1}{\lambda_c + 2\mu_c} \begin{Bmatrix} \varepsilon_{xx} \\ \varepsilon_{yy} \\ \varepsilon_{xy} \end{Bmatrix} - \frac{1}{\beta_c} \begin{Bmatrix} \bar{\alpha} \\ \bar{\alpha} \\ 0 \end{Bmatrix} T \right), \tag{29}$$

$$\begin{Bmatrix} \varepsilon_{xx} \\ \varepsilon_{yy} \\ \varepsilon_{xy} \end{Bmatrix} = \begin{bmatrix} \partial/\partial x & 0 \\ 0 & \partial/\partial y \\ \partial/2\partial y & \partial/2\partial x \end{bmatrix} \begin{Bmatrix} u_x \\ u_y \end{Bmatrix}$$

The local symmetric weak forms over the $J-$th local subdomain Ω_s^J write:

$$\int_{\Omega_s^J} v_J \left(\nabla . \boldsymbol{\sigma} \ - \frac{\rho}{\rho_c} \frac{\partial^2 \mathbf{u}}{\partial t^2} \right) d\Omega = 0 \tag{30}$$

Writing $v_J \nabla . \boldsymbol{\sigma} = \nabla . (v_J \boldsymbol{\sigma}) - \nabla v_J . \boldsymbol{\sigma}$ and using the divergence theorem, the local symmetric weak formulation becomes

$$\int_{\Gamma_{st}^J} v_J \tilde{\mathbf{t}} d\Gamma + \int_{\Gamma_{su}^J} v_J . \mathbf{n} d\Gamma + \int_{L_s^J} v_J . \mathbf{n} d\Gamma - \int_{\Omega_s^J} \left(\nabla v_J . + v_J \frac{\rho}{\rho_c} \frac{\partial^2 \mathbf{u}}{\partial t^2} \right) d\Omega = 0 \tag{31}$$

where $\tilde{\mathbf{t}}$ is the traction vector on the part of local boundary that coincides with the global traction boundary, Γ_t i.e. $\Gamma_{st}^J = \Gamma_t \cap \partial \Omega_s^J$, Γ_{su}^J is the part of local boundary that coincides with the global displacement boundary, Γ_u i.e. $\Gamma_{su}^J = \Gamma_u \cap \partial \Omega_s^J$, and $\mathbf{n}$ is the unit outward normal vector on Γ_{st}^J. The test function will be zero on the part of the local subdomain boundary that is completely inside the global domain. Thus, rearranging the unknown terms on the left side of Eq. 31, we obtain

$$\int_{\Omega_s^J} \left(\nabla v_J . \boldsymbol{\sigma} + v_J \frac{\rho}{\rho_c} \frac{\partial^2 \mathbf{u}}{\partial t^2} \right) d\Omega - \int_{\Gamma_{su}^J} v_J \boldsymbol{\sigma} . \mathbf{n} \, d\Gamma = \int_{\Gamma_{st}^J} v_J \tilde{\mathbf{t}} \, d\Gamma \tag{32}$$

Substituting Eq. 29 into Eq. 32, and using Eq. 3 for the approximation of the displacement vector, $\mathbf{u}$, with the trial displacement vector, $\mathbf{u}^h$, gives

$$\mathbf{M}_J \frac{d^2 \hat{\mathbf{u}}}{dt^2} + \mathbf{K}_J \hat{\mathbf{u}} = \mathbf{f}_J \tag{33}$$

In the preceding equation, $\hat{\mathbf{u}}$ is the fictitious value of the nodal displacement vector and $\mathbf{M}_J$, $\mathbf{K}_J$, $\mathbf{f}_J$ are the mass matrix, stiffness matrix and force vector of the J-th subdomain, respectively, which are defined as follows

$$\hat{\mathbf{u}} = \left\{ u_{x1} \quad u_{x2} \quad \cdots \quad u_{xN} \quad u_{y1} \quad u_{y2} \quad \cdots \quad u_{yN} \right\}^T,$$

$$\mathbf{K}_J = \frac{1}{\lambda_c + 2\mu_c} \int_{\Omega_s^J} \boldsymbol{\varepsilon}_J^M \mathbf{C} \mathbf{D}^M \boldsymbol{\Phi}^M d\Omega \ - \frac{1}{\lambda_c + 2\mu_c} \int_{\Gamma_{su}^J} v_J \mathbf{N} \mathbf{C} \mathbf{D}^M \boldsymbol{\Phi}^M d\Gamma$$

$$\mathbf{M}_J = \frac{1}{\rho_c} \int_{\Omega_s^J} v_J \rho \, \boldsymbol{\Phi}^M d\Omega \tag{34}$$

$$\mathbf{f}_J = \int_{\Gamma_{st}^J} v_J \tilde{\mathbf{t}} \, d\Gamma + \frac{1}{\beta_c} \int_{\Omega_s^J} \boldsymbol{\varepsilon}_J^M \mathbf{C} \boldsymbol{\alpha} T d\Omega - \frac{1}{\beta_c} \int_{\Gamma_{su}^J} v_J \mathbf{N} \mathbf{C} \boldsymbol{\alpha} T d\Gamma$$

where

$$\boldsymbol{\Phi}^M = \begin{bmatrix} \phi_1 & \phi_2 & \cdots & \phi_N & 0 & 0 & \cdots & 0 \\ 0 & 0 & \cdots & 0 & \phi_1 & \phi_2 & \cdots & \phi_N \end{bmatrix}$$

$$\mathbf{C} = \begin{bmatrix} \bar{\lambda} + 2\mu & \bar{\lambda} & 0 \\ \bar{\lambda} & \bar{\lambda} + 2\mu & 0 \\ 0 & 0 & 2\mu \end{bmatrix}, \quad \mathbf{N} = \begin{bmatrix} n_x & 0 & n_y \\ 0 & n_y & n_x \end{bmatrix}, \boldsymbol{\alpha} = \{\bar{\alpha} \quad \bar{\alpha} \quad 0\}^T$$

$$\mathbf{D}^M = \begin{bmatrix} \partial/\partial x & 0 & \partial/2\partial y \\ 0 & \partial/\partial y & \partial/2\partial x \end{bmatrix}^T, \boldsymbol{\varepsilon}_J^M = \begin{bmatrix} \partial v_J/\partial x & 0 & \partial v_J/\partial y \\ 0 & \partial v_J/\partial y & \partial v_J/\partial x \end{bmatrix} \tag{35}$$

Equation 33 consists of two ordinary differential equations with respect to time which are the equations of motion of the J-th local subdomain. Thus, a set of discretized coupled ordinary differential equations that represent the equation of motion over the whole global domain can be derived as

$$\bar{\mathbf{M}}\frac{d^2\hat{\mathbf{u}}}{dt^2} + \bar{\mathbf{K}}\hat{\mathbf{u}} = \bar{\mathbf{f}} \tag{36}$$

where

$$\bar{\mathbf{M}} = \begin{bmatrix} \bar{\mathbf{M}}_1^1 \\ \bar{\mathbf{M}}_2^1 \\ \vdots \\ \bar{\mathbf{M}}_{N_{tot}}^1 \\ \bar{\mathbf{M}}_1^2 \\ \bar{\mathbf{M}}_2^2 \\ \vdots \\ \bar{\mathbf{M}}_{N_{tot}}^2 \end{bmatrix}^{2N_{tot} \times 2N_{tot}}, \quad \bar{\mathbf{K}} = \begin{bmatrix} \bar{\mathbf{K}}_1^1 \\ \bar{\mathbf{K}}_2^1 \\ \vdots \\ \bar{\mathbf{K}}_{N_{tot}}^1 \\ \bar{\mathbf{K}}_1^2 \\ \bar{\mathbf{K}}_2^2 \\ \vdots \\ \bar{\mathbf{K}}_{N_{tot}}^2 \end{bmatrix}^{2N_{tot} \times 2N_{tot}}, \quad \bar{\mathbf{f}} = \begin{Bmatrix} f_1^1 \\ f_2^1 \\ \vdots \\ f_{N_{tot}}^1 \\ f_1^2 \\ f_2^2 \\ \vdots \\ f_{N_{tot}}^2 \end{Bmatrix}^{2N_{tot} \times 1}$$

in which, $\bar{\mathbf{M}}_J^1(\bar{\mathbf{M}}_J^2)$ is the assembled form of the first (second) row of the mass matrix of J-th subdomain, $\bar{\mathbf{K}}_J^1(\bar{\mathbf{K}}_J^2)$ is the assembled first (second) row of the stiffness matrix of the J-th subdomain, and f_J^1, f_J^2 are the first and second components of the force vector of the J-th subdomain, respectively.

3 Estimation of effective properties of FGMs

In this section, we briefly describe the method we use in this paper to estimate the thermo-mechanical material properties of functionally graded materials [Mori, T and Tanaka, K. (1973)], [Rosen, B W and Hashin, Z. (1970)] and [Hatta, H and

Taya, M. (1985)]. For estimating the elastic properties of graded microstructures with a well-defined continuous matrix and a discontinuous particulate phase, the Mori–Tanaka scheme is an effective technique. The Mori–Tanaka scheme assumes that the matrix phase is reinforced by spherical particles (the particulate phase). The effective local bulk modulus K and the shear modulus μ obtained by the Mori–Tanaka scheme for a random distribution of isotropic particles in an isotropic matrix are

$$\frac{K - K_m}{K_c - K_m} = \frac{V_c}{1 + 3\left(1 - V_c\right)\left(K_c - K_m\right)/\left(3K_m + 4\mu_m\right)} \tag{37}$$

$$\frac{\mu - \mu_m}{\mu_c - \mu_m} = \frac{V_c}{1 + \left(1 - V_c\right)\left(\mu_c - \mu_m\right)/\left(\mu_m + f_m\right)} \tag{38}$$

where

$$f_m = \mu_m \left(9K_m + 8\mu_m\right)/6\left(K_m + 2\mu_m\right) \tag{39}$$

In the above, subscripts m and c denote the values of a quantity for metal and ceramic constituents of the functionally graded domain, V_c is the volume fraction of ceramic, and $V_m = 1 - V_c$ is the volume fraction of the metal constituent, respectively. The volume fraction of ceramic constituent varies through the x-direction and is assumed to obey the following relation

$$V_c = \left(x/l_x\right)^p \tag{40}$$

where parameter p characterizes the variation in ceramic content and the material distribution throughout the geometry of the domain. Using the following relation, the other mechanical material properties can be obtained

$$\lambda = K - \frac{2\mu}{3}, \quad E = \frac{9K\mu}{3K + \mu}, \quad \nu = \frac{3K - 2\mu}{2\left(3K + \mu\right)} \tag{41}$$

The mass density ρ at a point is obtained by the simple rule of mixtures as

$$\rho = \rho_m V_m + \rho_c V_c \tag{42}$$

The effective heat capacity per unit volume, ρc, of the functionally graded domain is also assumed to follow the rule of mixtures

$$\rho c = \rho_m c_m V_m + \rho_c c_c V_c \tag{43}$$

The effective thermal conductivity, k, is computed from the following relation proposed by Hatta and Taya [Hatta, H and Taya, M. (1985)]

$$\frac{k - k_m}{k_c - k_m} = \frac{V_c}{1 + (1 - V_c)(k_c - k_m)/3k_m} \tag{44}$$

and the effective coefficient of thermal expansion α is given by [Rosen, B W and Hashin, Z. (1970)]

$$\frac{\alpha - \alpha_m}{\alpha_c - \alpha_m} = \frac{1/K - 1/K_m}{1/K_c - 1/K_m} \tag{45}$$

4   The Time Integration Scheme

In the present work, Eq. 21 is integrated with respect to time t by the Crank-Nicholson method

$$\hat{\mathbf{T}}_{\tau+\Delta\tau} = \hat{\mathbf{T}}_\tau + \frac{\Delta\tau}{2}\left(\dot{\hat{\mathbf{T}}}_\tau + \dot{\hat{\mathbf{T}}}_{\tau+\Delta\tau}\right) \tag{46}$$

Since the Crank-Nicholson method is unconditionally stable, the time step size may be determined by the desired accuracy. To solve Eq. 36, the Houbolt method is applied. In the Houbolt finite difference scheme [Houbolt, J C. (1950)] the acceleration is expressed as

$$\frac{d^2\hat{\mathbf{u}}_{\tau+\Delta\tau}}{dt^2} = \frac{2\hat{\mathbf{u}}_{\tau+\Delta\tau} - 5\hat{\mathbf{u}}_\tau + 4\hat{\mathbf{u}}_{\tau-\Delta\tau} - \hat{\mathbf{u}}_{\tau-2\Delta\tau}}{\Delta\tau^2} \tag{47}$$

where $\Delta\tau$ is the time step.

Upon substitution of Eq. 46 into Eq. 21 and Eq. 47 into Eq. 36, we get the system of algebraic equations for the unknown fictitious nodal temperatures and displacements as

$$\begin{aligned}
(\bar{\mathbf{H}} + \frac{2}{\Delta\tau}\bar{\mathbf{R}})\hat{\mathbf{T}}_{\tau+\Delta\tau} &= \bar{\mathbf{P}}_{\tau+\Delta\tau} + \frac{2}{\Delta\tau}\bar{\mathbf{R}}\hat{\mathbf{T}}_\tau + \bar{\mathbf{R}}\dot{\hat{\mathbf{T}}}_\tau \\
\left(\frac{2}{\Delta\tau^2}\bar{\mathbf{M}} + \bar{\mathbf{K}}\right)\hat{\mathbf{u}}_{\tau+\Delta\tau} &= \bar{\mathbf{M}}\frac{1}{\Delta\tau^2}(5\hat{\mathbf{u}}_\tau - 4\hat{\mathbf{u}}_{\tau-\Delta\tau} + \hat{\mathbf{u}}_{\tau-2\Delta\tau}) + \bar{\mathbf{f}}_{\tau+\Delta\tau}
\end{aligned} \tag{48}$$

The value of the time step has to be appropriately selected with respect to material parameters (wave propagation speed) and the time dependence of the boundary conditions.

5 Numerical experiment and discussion

5.1 *Validation in the homogeneous isotropic case*

We first compare our results with an analytical solution in the case of a homogenous domain to validate the formulation. In the subsequent sections, we show results for transient and dynamic thermo-elastic deformations of 2D FG domains. In the remainder of this section, we provide a comparison between results obtained based on the present formulation and the analytical evolution of temperature within a 2D homogeneous isotropic domain subjected to mixed thermal boundary conditions. A two-dimensional homogeneous square domain with length $l_x = 1\,m$ and width $l_y = 1\,m$ is considered. It is assumed that the temperature at both edges parallel to the y-axis is prescribed, see Fig. 3. The left-hand side is kept at zero temperature while the right-hand side experiences a Heaviside step time variation of temperature, i.e. $T(l_x,t) = H(t)$. On the lateral (horizontal) sides, the domain is insulated. An analytical solution can easily be obtained by the method of separation of variables and reads

$$T(x,t) = \frac{x}{l_x} + \frac{2}{\pi} \sum_{n=1}^{\infty} \frac{\cos n\pi}{n} \sin\left(\frac{n\pi x}{l_x}\right) \times \exp\left(-\frac{\kappa n^2 \pi^2}{l_x^2}t\right) \tag{49}$$

This solution is used to measure the accuracy of the present numerical method. Numerical results are computed at four different locations along the x-axis, i.e. x=0.2, 0.4, 0.6 and 0.8. In Fig. 4 a comparison between the simulated and analytical temperature evolution at different locations along the x-axis, are presented. It can be observed in the figure that an excellent agreement between numerical and analytical results is obtained.

Remark In this study 30 nodes were used in the x- direction and 5 nodes were used in the y-direction.

5.2 *Validation of the thermal stress solution in a functionally graded material*

In this section, we compare our formulation with some data from the literature to validate the thermal stress solution. For this purpose, we consider a simply supported functionally graded beam of rectangular cross section $(b \times a)$ and length L, with exponentially varying properties across the beam thickness as

$$\begin{aligned} E(y) &= E_0 \exp(\xi_1 y/a) \\ \alpha(y) &= \alpha_0 \exp(\xi_2 y/a) \end{aligned} \tag{50}$$

Here $E_0 = 70\,GPa$ is a reference Young's modulus and $\alpha_0 = 23 \times 10^{-6\,\circ}C^{-1}$ is a reference thermal expansion coefficient. In this case, $\xi_1 = 1.7$, $\xi_2 = -1.13$
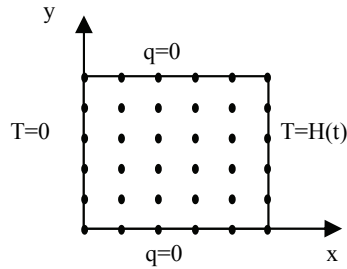
Figure 3: Sketch of the problem domain for validation of the temperature distribution computations in an isotropic homogeneous domain. Boundary conditions are also shown. Here, q denotes the heat flux and H the Heaviside step function.
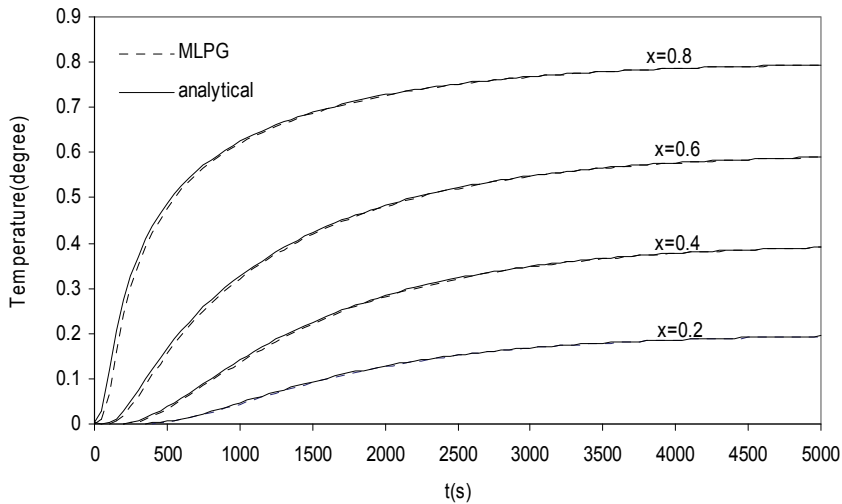
Figure 4: Time variation of temperature in an isotropic homogeneous 2D domain for $N_x = 30$ by $N_y = 5$ array of nodes.

$a = 0.1$, $b = 1$ and Poisson's ratio $v = 0.3$ is considered to be constant across the thickness. The beam is initially at temperature T_0. This uniform temperature is "slowly" raised to T_f, where the temperature difference is $\theta = T_f - T_0 = 1 \circ C$.

In Fig. 5 the normal stress σ_{xx} across the thickness of the beam provided by the analytical solution of Reference [Hetnarski, R B and Eslami, M R. (2008)] and the present MLPG formulation have been compared. It can be seen that the MLPG result agrees very well with that from the analytical solution. Note that the analytical solution is based on Euler-Bernoulli assumption and the MLPG solution is based

on classical thermo-elasticity equations.

Remark detailed studies were performed to show that the solution converges with mesh refinement, but are not reported here for conciseness. The interested reader is referred to the extensive theoretical and numerical work [Kim, H G and Atluri, S N., (2000)], where details on the numerical behavior of the MLPG method are provided. The results of Fig. 5 are obtained with a total of 100 nodes, i.e. 10 nodes through the length and height of the beam.
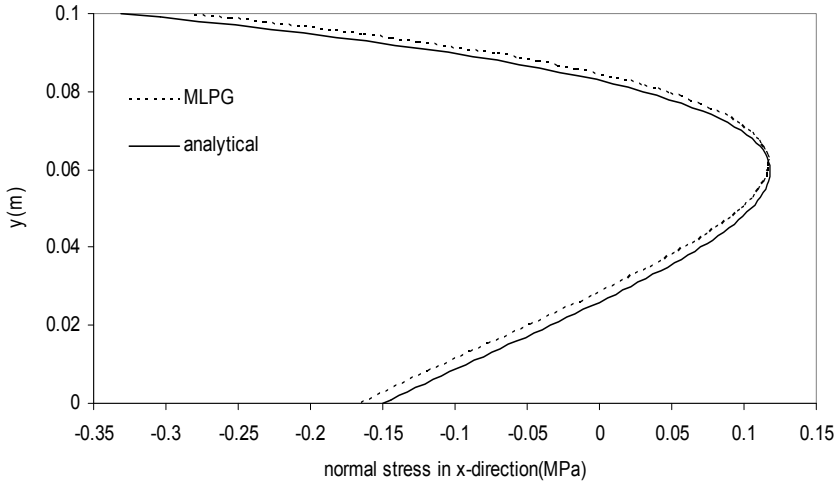
Figure 5: Normal stress σ_{xx} along the cross section at the middle of the FG beam.

5.3 Dynamic thermo-elastic simulation of functionally graded materials

In this section, we employ the proposed numerical technique to analyze the dynamic thermo-elastic behavior of rectangular functionally graded domains. To do so, we consider a two dimensional FG square domain with non-dimensional length $l_x = 1$ and width $l_y = 1$ subjected to the following boundary conditions (cf. Fig. 6):

Mechanical B.C. and I.C.		Thermal B.C. and I.C.
		$\mathbf{q}(x,0,t).\mathbf{n} = 0$
$\mathbf{u}(0.y,t) = 0$		$\mathbf{q}(x,l_y,t).\mathbf{n} = 0$
$\mathbf{u}(x,y,0) = 0$		$T(0,y,t) = 0$
$\frac{\partial \mathbf{u}(x,y,0)}{\partial t} = 0$		$T(l_x,y,t) = 100f(t)$
The free boundaries are assumed to be traction free		$T(x,y,0) = 0$

where $f(t) = 1 - e^{-5\frac{C_1^2}{\kappa_m}t}$ and C_1 and κ_m are defined in Eq. 12.

Insulated and traction free boundary
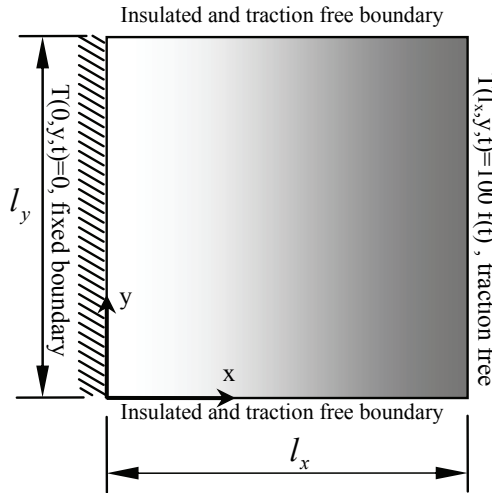
Figure 6: Thermal and mechanical boundary conditions of a two dimensional FG domain. The ceramic-rich region is on the right-hand side of the plate.

To carry out the numerical studies, Aluminum (Al) and Alumina (Al$_2$O$_3$) are considered as ceramic and metal constituents, respectively, and the following material properties and computational parameters are chosen

Al : $\rho_m = 2707\,\text{kg / m}^3$, $c_m = 903\,\text{J / kg}°\text{C}$
$k_m = 204\,\text{W / m}°\text{C}$, $\alpha_m = 23 \times 10^{-6}\,/\,°\text{C}$
$E_m = 70\,\text{GPa}$, $v_m = 0.3$

Al$_2$O$_3$: $\rho_c = 3800\,\text{kg / m}^3$, $c_c = 765\,\text{J / kg}°\text{C}$
$k_c = 10.4\,\text{W / m}°\text{C}$, $\alpha_c = 7.4 \times 10^{-6}\,1\,/\,°\text{C}$
$E_c = 380\,\text{GPa}$, $v_c = 0.17$

$m = 6$, $r_I^x = 3h_I^x$, $r_I^y = 3h_I^y$, $\Delta\tau = 0.05$, $N_x = N_y = 31$

where h_I^x, is the distance from node I to the nearest neighbor node in the x-direction and h_I^y is the distance from node I to the nearest neighbor in the y-direction. Also, E is the Young's modulus and v is the Poisson's ratio. With the use of uniform node generation, 961 nodes with 31 nodes in the x-direction and 31 in the y-direction are generated to cover the domain, and $r_I^x = r_I^y = 0.1$. The size of support of the test function v_I, is $\left[h_I^x \times h_I^y\right]$ and the size of domain of definition of the shape function is chosen as $\left[3.5\,h_I^x \times 3.5\,h_I^y\right]$. Also, 144 quadrature points are employed to evaluate

area integrals and 100 integration points are used for the trapezoid integral method employed to evaluate line integrals.

Remark these high-order quadrature schemes are required because the moving least squares (MLS) shape functions defined in Section 2.1. are non-polynomial. This is one of the drawbacks of MLS-based "meshfree" methods, since the need for high order quadrature increases the computational time significantly compared to standard finite element methods which rely on low-order polynomial interpolants. Nonetheless, the added advantages provided by extra smoothness and the simplicity with which adaptivity can be performed can offset these disadvantages. It is important to note that the influence of point placement on the quality of the MLS approximation is in general not very well understood, and requires further study [Nguyen, V P; Rabczuk, T; Bordas, S; Duflot, M. (2008)].

Note that the value of p controls the material composition. Two extremes are attained for $p = 0$ (pure Alumina/ceramic) and p approaching to positive infinity (pure Aluminum/metal).

The steady state temperature distribution along the x-axis is shown in Fig. 7, from which the following conclusions can be drawn:

- Higher values of p (i.e. larger Aluminum volume fraction in the domain) decrease the temperature on the left-hand side of the domain, and lead to larger temperature gradients on the right-hand side. In this case (for instance $p = 5$ in Fig. 7, the temperature distributes less evenly throughout the domain;

- For a homogeneous material, i.e. $p = 0$, the steady state temperature distribution is almost exactly linear for a, which is the expected solution to Laplace equation to which the problem at hand degenerates in this case.

Fig. 8 depicts the variation of the temperature at points located on vertical mid-line of the domain for different values of the power law index, p. One key observation can be made from these results: Aluminum has larger thermal diffusivity coefficient than Alumina, which means that the temperature rise in pure Aluminum (case p=inf.) is faster than for any other material distribution. This is clearly identified in Fig. 8 where it is apparent that for larger values of the power law index, p, steady state is attained faster (5 times faster for the pure Aluminum case than for p=0.5). Therefore, in the case of thermal shock loads, application of FGMs can be considered as a material strategy to avoid distribution of undesired thermally induced stresses, which can result in void growth and crack propagation through the structure.

The heat flux variation at different positions in the domain is shown in Fig.9 for the case $p = 0.5$. From this figure, the following conclusions can be inferred:
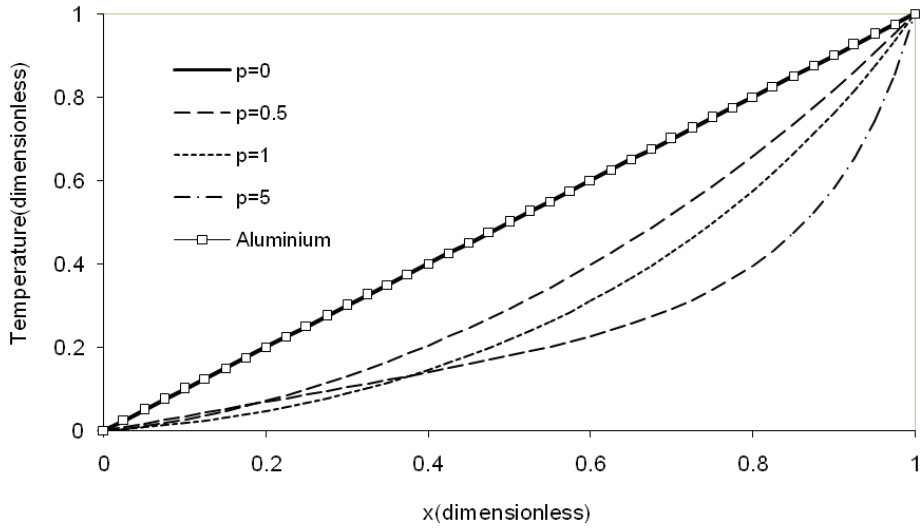
Figure 7: Distribution of steady state temperature along the x-direction for various material compositions. Large values of *p* indicate large volume fractions of metal.
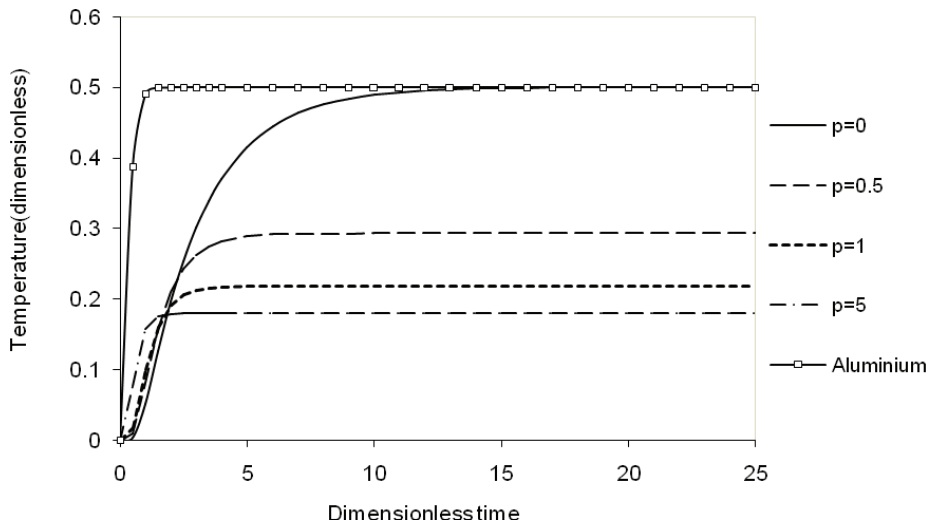

Figure 8: Time variation of temperature at points lying along the vertical mid-line (x=0.5) of the domain. The Aluminum case is equivalent to *p* approaching towards positive infinity.

- At the primary stages of thermal excitation, the boundary where the thermal load is applied experiences a large heat flux magnitude;

- At any given time, the magnitude of the heat flux decreases with distance from the heat source;

- At any given point along the domain, the same steady state heat flux magnitude is reached;

- The manner in which steady state is reached is not the same throughout the domain. For points located further away from the heat source, steady state is reached monotonously (the heat flux continuously decreases from 0 to the (negative) steady state value). On the contrary, for points located close to the heat source, the heat flux initially overshoots the steady state value, and the steady state is not reached monotonously ($x = 0.9$ and $x = 1.0$) in the figure.
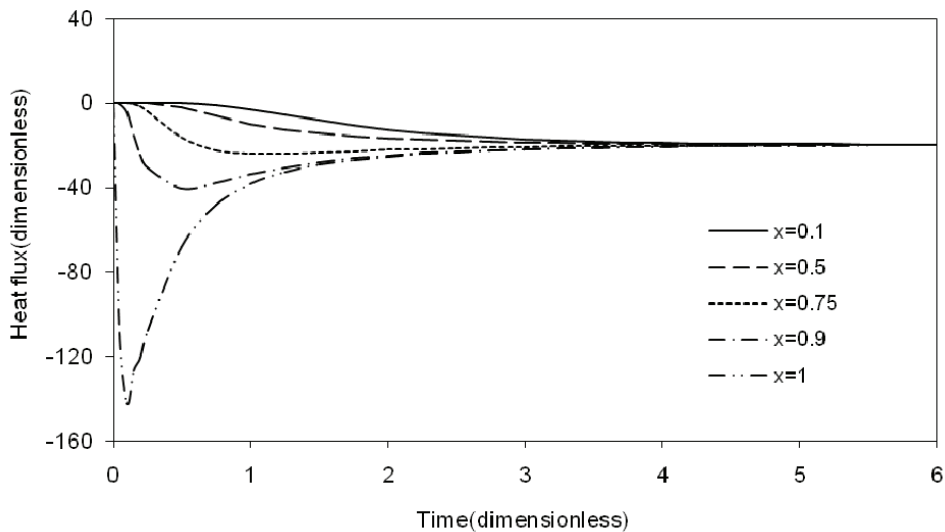
Figure 9: Time variation of heat flux at some points of FG domain (p=0.5). Recall that the thermal excitation is applied at $x = 1$. It is clear from this figure that the largest heat fluxes are observed in the vicinity of the thermal excitation boundary. Throughout the domain, these dimensionless heat fluxes reach a steady state value around negative 20.

Fig. 10 shows the steady state heat flux in the x-direction for two types of domain: an FGM domain and a domain made of two metal and ceramic layers. In the two
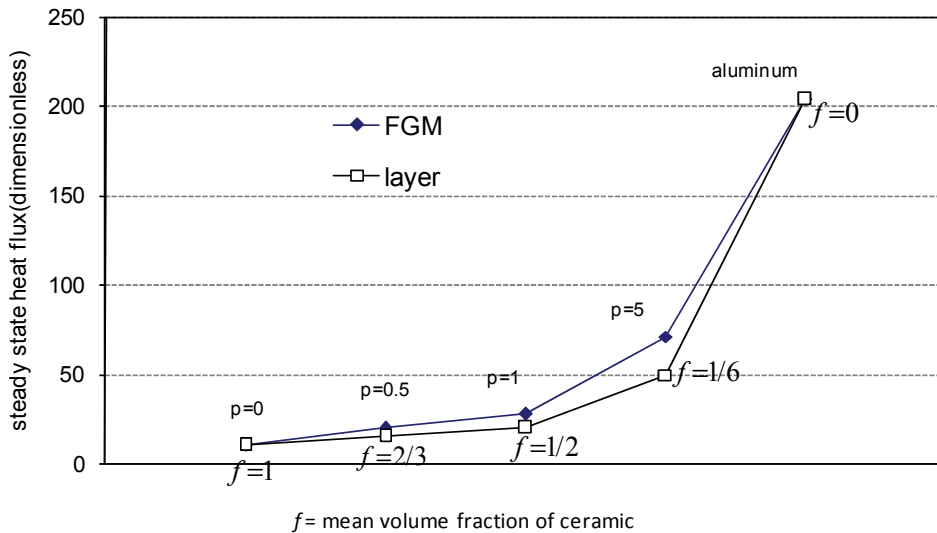
Figure 10: Comparison of the steady state heat flux for a functionally graded do-
main and a domain with only two Aluminum and Alumina layers. The comparison
is shown for various volume fractions, f, of ceramic material. It is apparent that
the steady state heat flux is largest for pure Aluminum ($p=inf$), smallest for pure
ceramics ($p = 0$), and always larger for the functionally graded material than for
the bi-material layers (for the same volume fraction of ceramics).

layer domain, the Aluminum layer is located on the left-hand side and the ceramic
layer is located on the right-hand side. The temperature and heat flux both reach
steady state. From Fig. 10, the following conclusions can be drawn:

- The steady state heat flux for the pure Aluminum domain is approximately
  204, which is, as expected, greater than those obtained for all other domains;

- By increasing the Alumina volume fraction ($p = 5$), the steady state heat flux
  in the FG domain decreases to 70.96, and to 49.75 in the two layer material.
  This shows that adding a small amount of ceramic as a thermal barrier can
  reduce the heat flux considerably and it also shows that heat flux in a two
  layer domain is smaller than heat flux in an FG domain with same mean
  volume fractions of components.

Remark The mean volume fraction of ceramic in an FGM domain is obtained as follows

$$f = \frac{1}{l_x} \int_0^{l_x} (x/l_x)^p dx \tag{51}$$
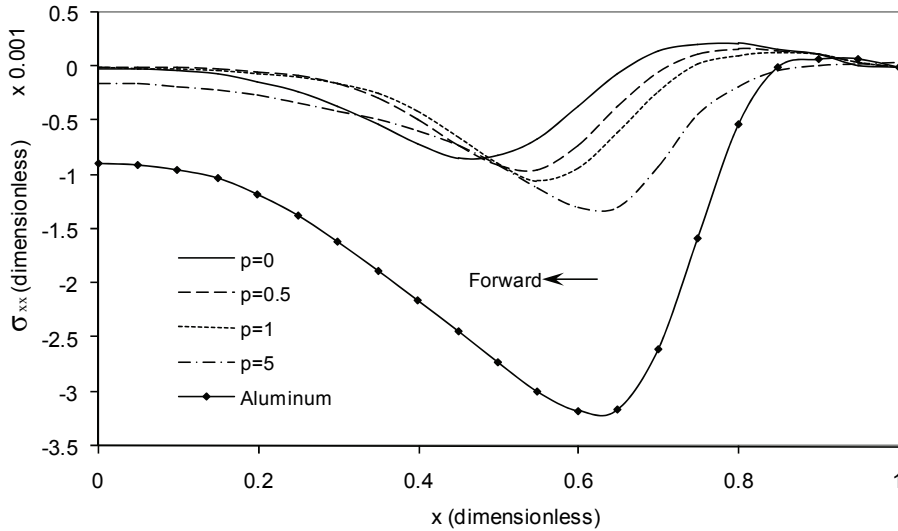
Figure 11: Distribution of σ_{xx} along the horizontal mid-line of domain (y=0.5) at dimensionless time t=0.7.

The distribution of thermal stress, σ_{xx}, along the horizontal mid-line of the domain at dimensionless time t=0.7 for five various cases of material distributions (p=0, 0.5, 1, 5 and ∞) is shown in Fig. 11. The following conclusions can be inferred from these results:

- For the pure ceramics domain (p=0), the σ_{xx} stress component propagates within the domain at a larger speed than for the other material compositions. By increasing the amount of Aluminum, the stress wave speed decreases. This is explained by smaller elastic modulus of Aluminum compared to Alumina. The larger thermal diffusivity coefficient of Aluminum compared to Alumina decreases the rising time for the transient thermal stress σ_{xx};

- When p increases, due to the larger thermal expansion coefficient of Aluminum and a greater energy absorption into the body, larger amplitudes of

σ_{xx} are obtained. According to Fig. 11, even a very small amount of ceramics (p=5) in the material effectively acts as a thermal barrier, leading to a considerably lower thermal stress amplitude.
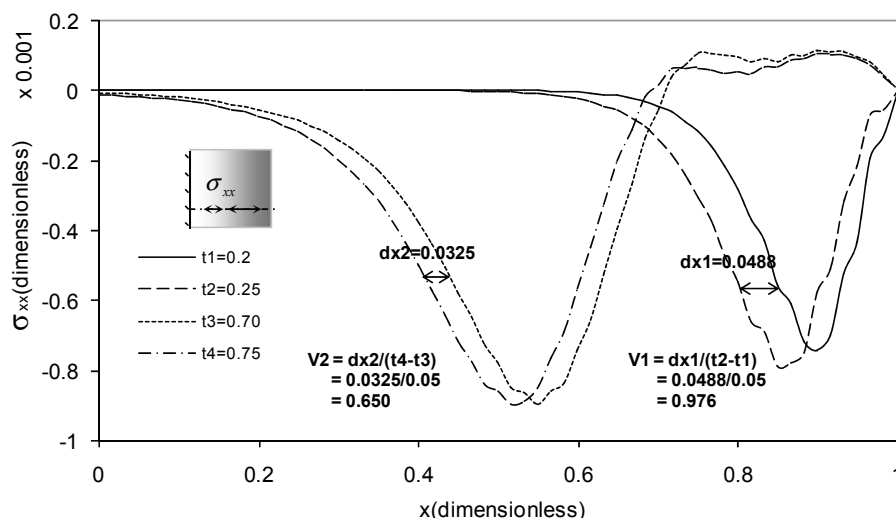
Figure 12: Longitudinal propagation of stress component σ_{xx} and variation of mean speed of the wave along line y=1/6 of the FG domain when p=1. The ceramics rich side is on the right-hand side of the domain.

The longitudinal wave propagation of σ_{xx} in an FG domain with power index $p = 1$ is shown in Fig. 12. The main conclusion of this figure is that the mean speed of stress wave propagation near the ceramic rich side (right-hand side) is larger than that in the vicinity of metal rich side (left-hand side). The reason for this is that near the ceramic rich side, the elastic modulus of the FG material is larger, which results in larger elastic wave speed.

Figures 13-15 show transverse wave propagation of σ_{xx} along the y direction for p=1 at x=0, 0.5 and for p=5 at x=0.5. According to the results shown in Figs. 13, 14, the transverse wave speed at x=0.5 is about $\bar{V} = 0.667$ and at x=0 is about $\bar{V} = 0.5$ for p=1. As shown in Fig. 15, the transverse wave speed on x=0.5 is about $\bar{V} = 0.33$ for p=5. It indicates that with increase of the amount of Aluminum in the FG material, the speed of transversely propagating stress waves decreases, which can be attributed to a decrease in effective shear modulus of FGM in presence of more metal constituent.
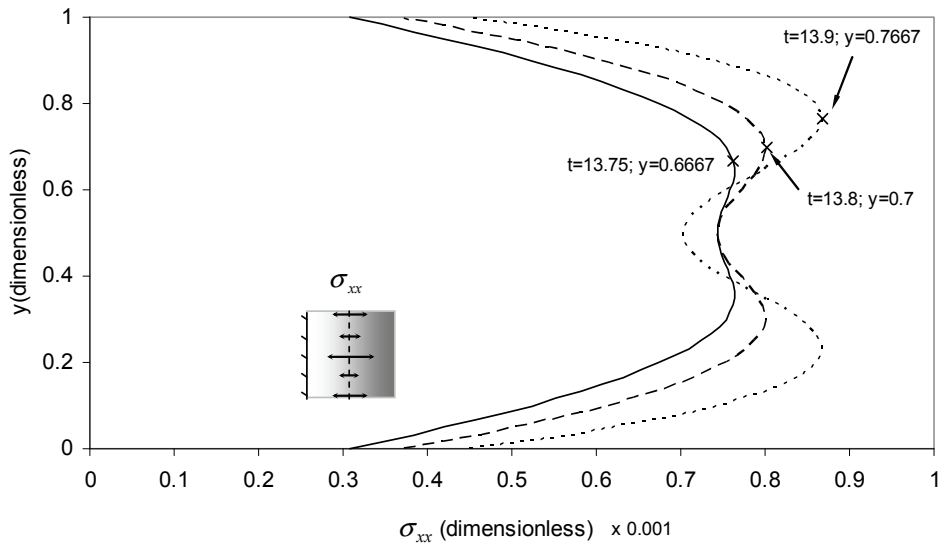
Figure 13: Transverse wave propagation of σ_{xx} along y direction at x=0.5 of the FG domain (p=1); t is dimensionless time.
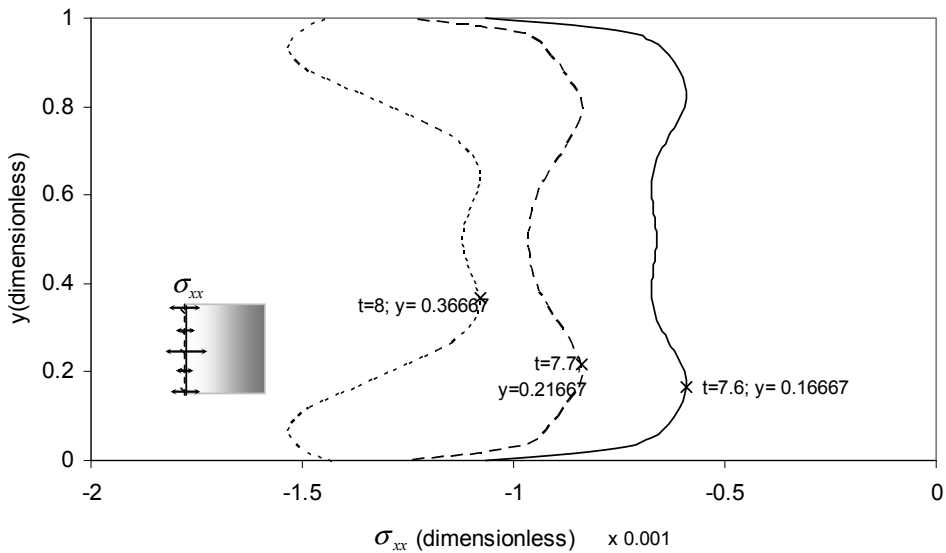
Figure 14: Transverse wave propagation of σ_{xx} along y direction on the left-hand side (x=0) of FG domain (p=1); t is dimensionless time.
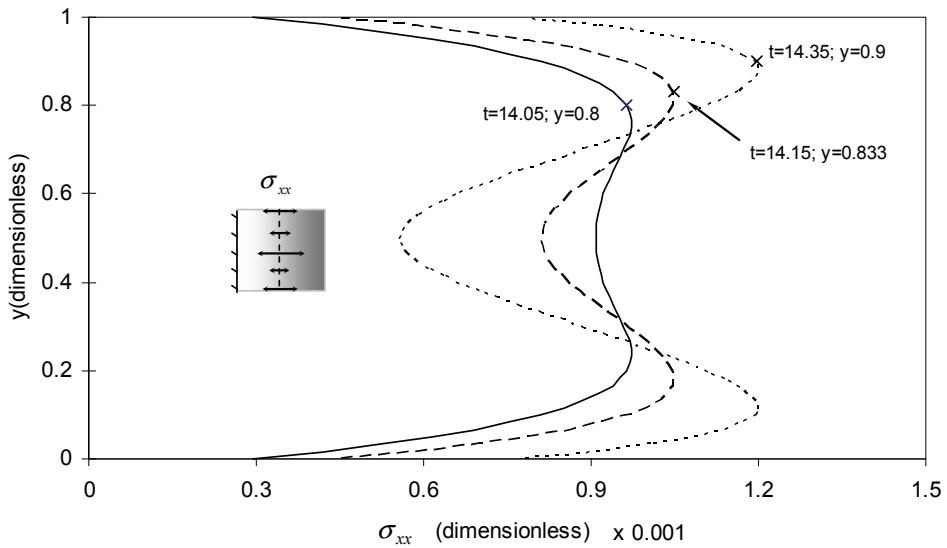
Figure 15: Transverse wave propagation of σ_{xx} along y direction at x=0.5 of the of FG domain (p=5); t is dimensionless time.
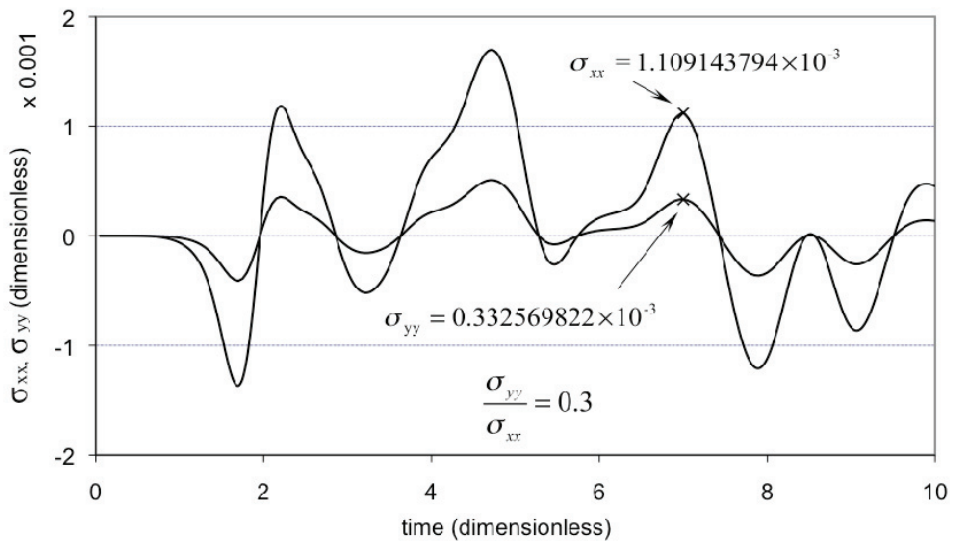

Figure 16: Variation of σ_{xx} and σ_{yy} at point (0,0.5) of the FG domain (p=1) and Poisson's ratio effect.

Fig. 16 shows the time evolution of the x- and y- components of the stress in the domain. The following conclusions can be drawn from these results:

- Due to the thermal and mechanical boundary conditions, the displacement in the y direction of all points on the x=0 edge of the domain are zero; accordingly, the dynamic change of σ_{yy} is only affected by the dynamic variation of σ_{xx} because of the Poisson's ratio effect. For all values of power index, $p > 0$, at point (0, 0.5) which is located at Aluminum rich side, the stress ratio equals to 0.3, i.e. the Poisson's ratio of Aluminum;

- The first stress peak is in compression while the second one is in tension. Due to the fixed and free boundaries on the left and right hand sides of the domain and their effects on reflection of the waves, it can be seen in the figure that the sign of stresses successively change.
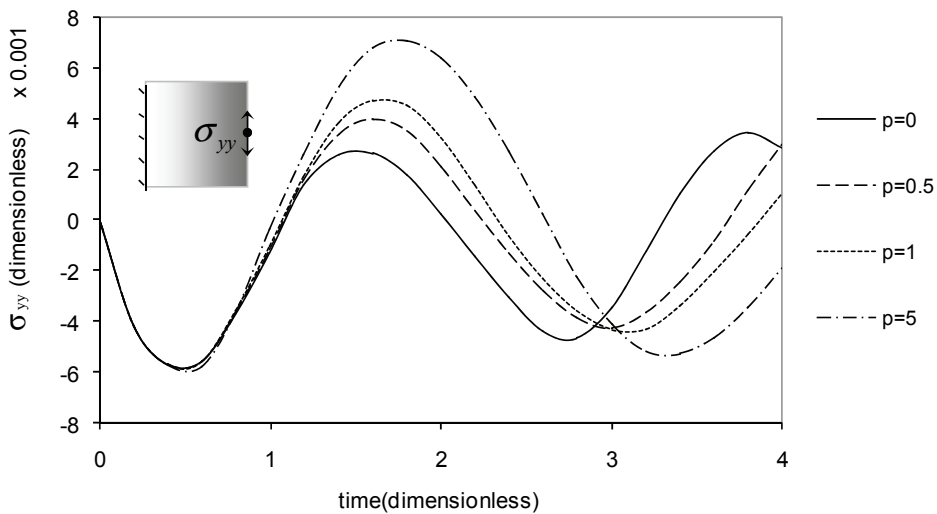
Figure 17: Variation of σ_{yy} at point (1,0.5) for several values of p at primary stages of thermal excitation.

The time history of σ_{yy} at point (1, 0.5) for several values of p is plotted in Fig. 17. According to the results shown in this figure, up to time t~0.75, the normal stress σ_{yy} variation in the ceramic rich side of the FGM domain is the same as for the fully ceramic domain. By increasing the power law index value, the Aluminum volume fraction increases and, consequently, the coefficient of thermal expansion increases

in the vicinity of point (1,0.5), which influences the stress magnitude at this point. It can be seen in the figure that the amplitude of σ_{yy} increases with p.

The thermal stress σ_{yy} distribution along the vertical mid-line of the FG domain (x=0.5) for several values of p is plotted in Fig. 18 at dimensionless time t=0.7. These results show that

- The ceramic domain experiences the smallest σ_{yy} amplitude, and that by increasing the amount of Aluminum, σ_{yy} increases. Alumina (ceramics) has a smaller thermal expansion coefficient than Aluminum and considering the results shown in Fig. 8, the mid-line temperature in the pure ceramics case is less than for any other FG material at dimensionless time t=0.7, which explains the small thermal stress magnitude (σ_{yy}) in the case where p=0;

- At the top and bottom of the domain (y=0, y=1), σ_{yy} is equal to zero and the boundary conditions are indeed satisfied.
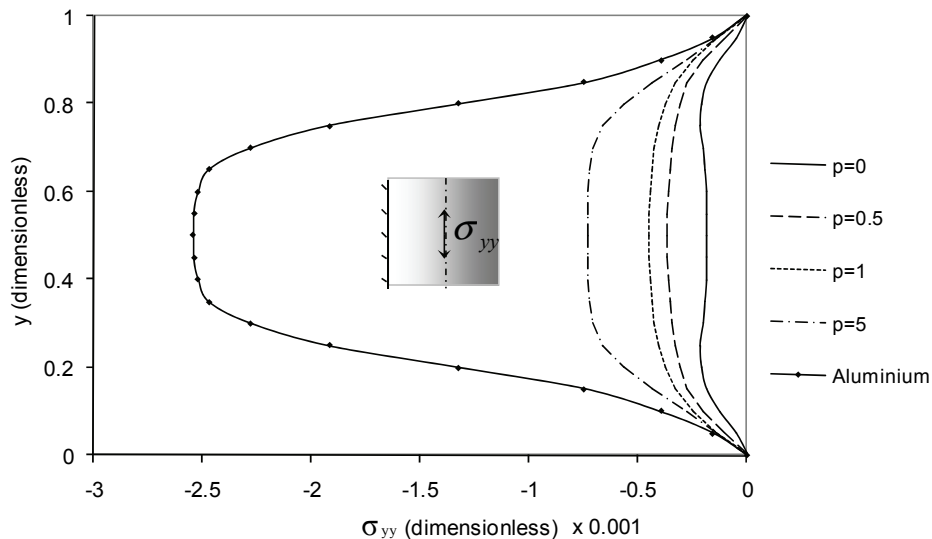
Figure 18: Thermal stress σ_{yy} distribution along vertical mid-line (x=0.5) of the domain for several values of p at dimensionless time t=0.7.

At dimensionless times t=0.7 and t=1, the transverse distribution of σ_{yy} on the horizontal mid-line of the domain (y=0.5) is plotted in Figs. 19a. and 19b, respectively. It can be concluded from the results shown in these figures that the speed of trans-

verse wave propagation of σ_{yy} in the pure ceramics domain is faster than that in the FG domains and that this speed decreases with increasing p.

Transverse wave propagation of σ_{yy} along the horizontal mid-line (y=0.5) of the FG domain (p=1) at several dimensionless times t=0.65, 0.85, 1.05, and 1.45 is shown in Fig. 20. The wave front can be clearly detected in the figure.

Thermal stress σ_{yy} distribution along the y-direction at the ceramic rich side of the FG domain (p=1) is shown in Fig. 21. This figure shows that at the top and bottom of fully ceramic edge the thermal stress σ_{yy} is equal to zero and the stress distribution along this edge successively changes from positive to negative values. It can be inferred from this figure that:

- The maximum value of σ_{yy} occurs at the midpoint of the thermally loaded edge;

- Since all the points along this edge experience the same thermal load, the normal stress σ_{yy} does not propagate as a dilatational wave in the y-direction.

Distributions of thermal stress σ_{xx} at dimensionless times t=0.35, 0.75 in a fully Aluminum domain and a FG domain are shown in Figs. 22 and 23, respectively. In Figs. 22a and 23a two arrows are shown which indicate the path of the two peaks and in Figs. 22b and 23b two peaks are shown that move in the x and y directions simultaneously. The propagation of the σ_{xx} peak in the x-direction is a longitudinal propagation and its propagation in the y-direction is a transverse propagation. Therefore, the total speed of the normal stress wave in a 2D domain is results in the combination of longitudinal and transverse wave propagation.

Contours of the peak points of the σ_{xx} distribution are shown in Figs. 24 and 25 at dimensionless times t=0.35, 0.55, 0.75, 0.95. According to the results shown in Figs. 24 and 25, the speed of the σ_{xx} wave propagation in the x-direction is larger than that in the y-direction. Also, comparing the σ_{xx} longitudinal and transverse wave speeds in the fully Aluminum domain and the FG domain shown in Figs 24 and 25 reveals that both longitudinal and transverse wave speeds in pure Aluminum are smaller and that in the FG domain they are position dependent.

The time history of the variations of the displacement in the x-direction, u_x, at point (1,0.5) and the displacement in the y-direction, u_y, at point (1,1) for various values of p are plotted in Figs. 26 and 27, respectively. The maximum displacement occurs in the Aluminum domain while the full ceramics domain shows minimum displacement amplitude in both figures. It can be concluded from the results for the pure Aluminum case, $p = \infty$, and the case with small amount of ceramic constituent, p=5, that the displacement amplitude considerably decreases so that it approaches the displacement amplitude of the pure ceramic domain, $p = 0$. As shown
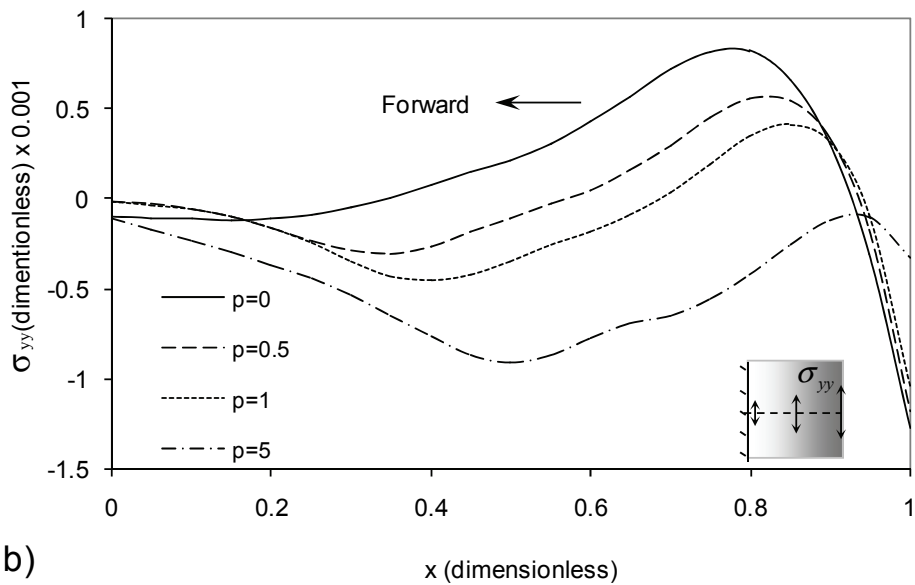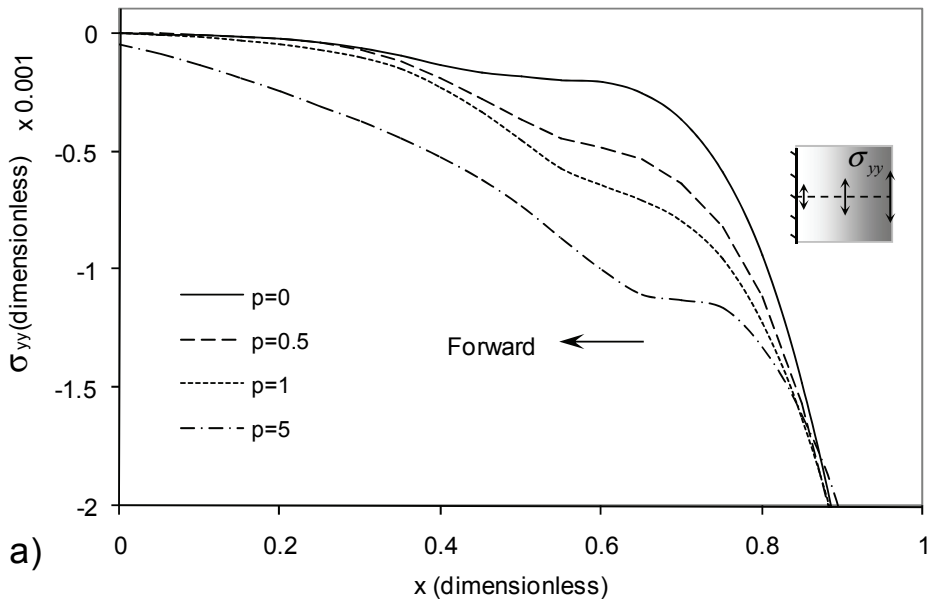
Figure 19: Thermal stress σ_{yy} distribution along horizontal mid-line (y=0.5) of the domain for several values of p: a) at dimensionless time t=0.7 b) at dimensionless time t=1.
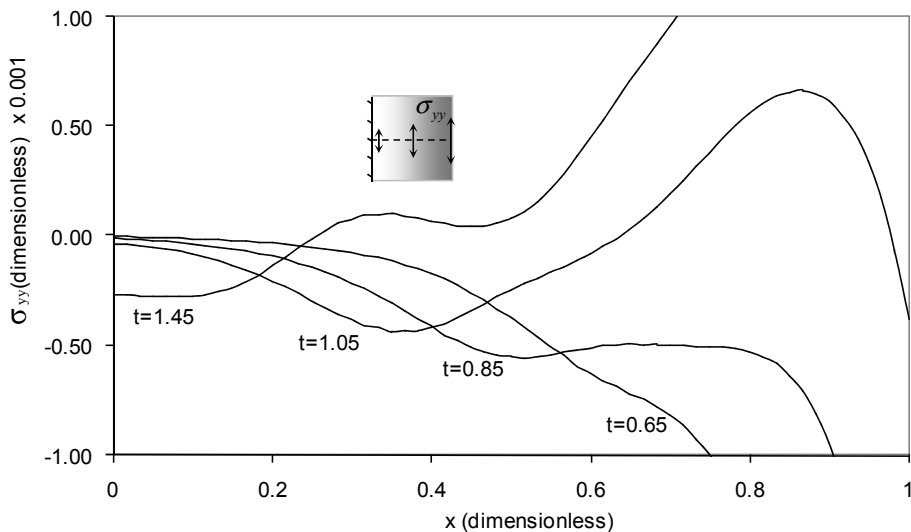
Figure 20: Transverse wave propagation of σ_{yy} along horizontal mid-line (y=0.5) of the FG domain for p=1; t is dimensionless time.
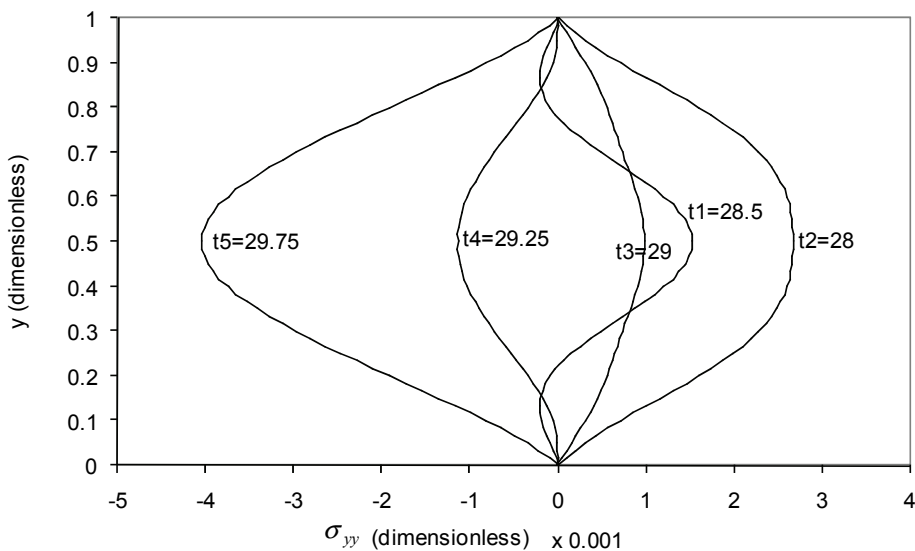

Figure 21: Thermal stress σ_{yy} distribution along the ceramic rich side, x=1 of the FG domain (p=1) at several times; t is the dimensionless time.
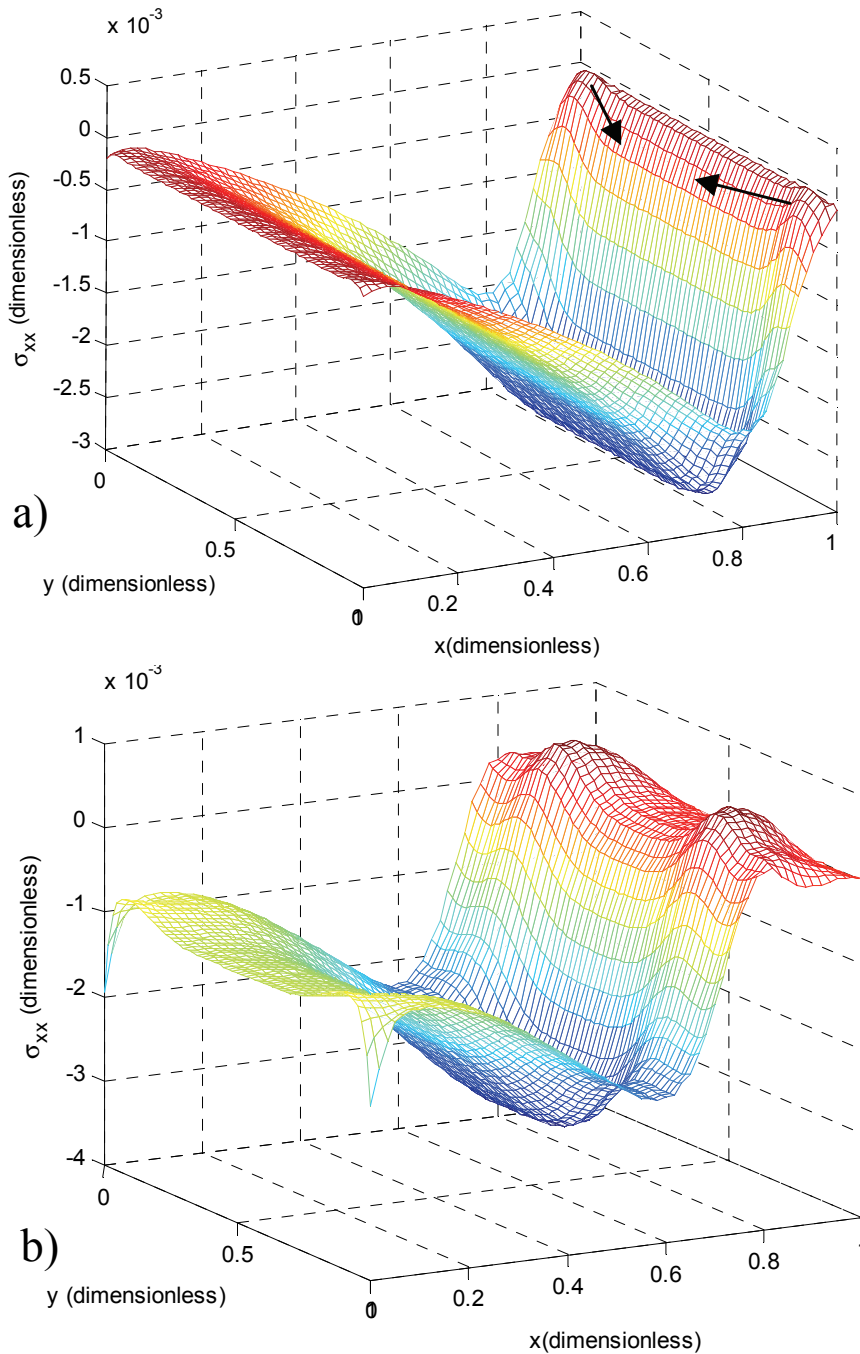
Figure 22: Thermal stress σ_{xx} distribution on 2D fully Aluminum domain at dimensionless times a) t=0.35 b) t=0.75.
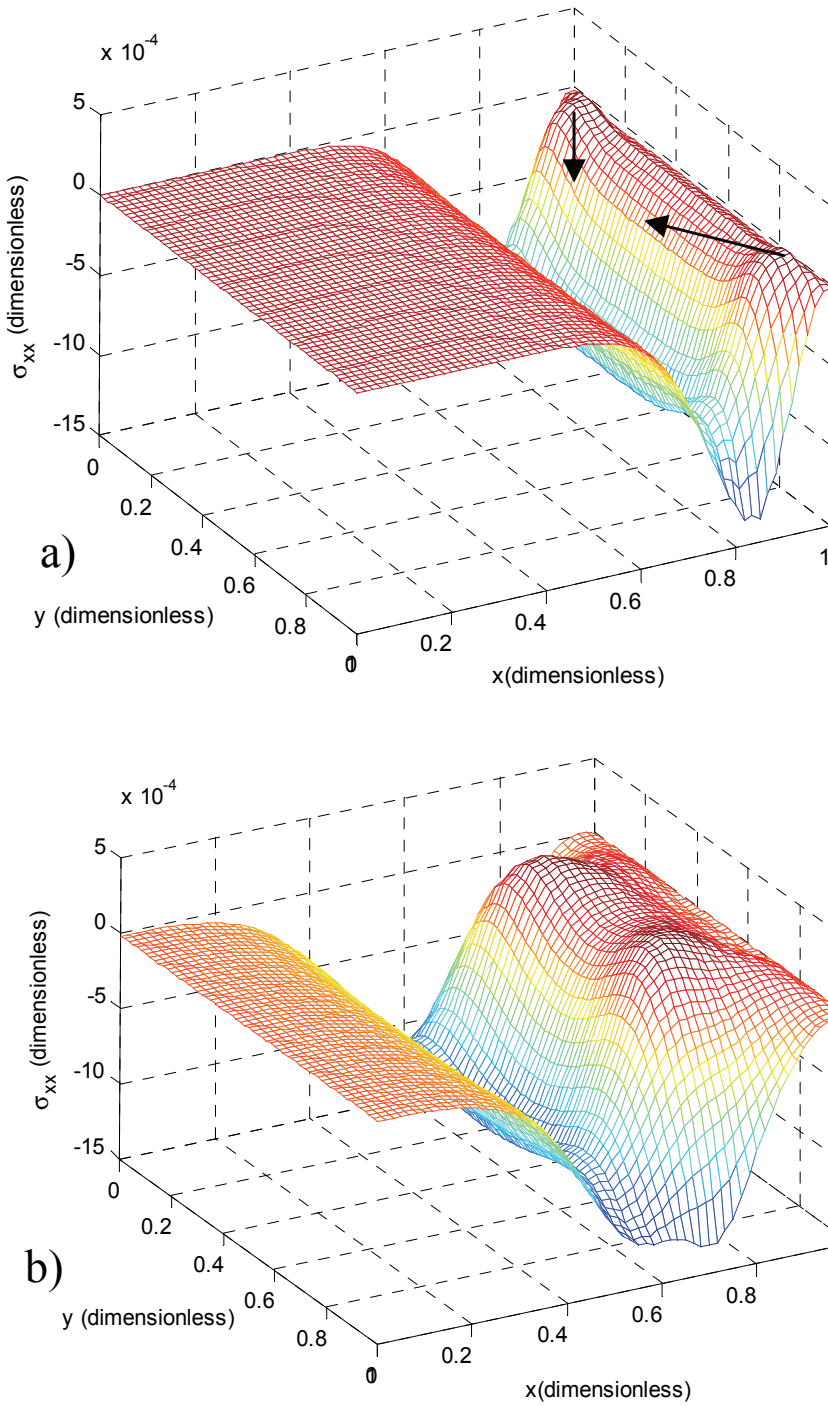
Figure 23: Thermal stress σ_{xx} distribution on a 2D FG domain (p=1) at dimensionless times a) t=0.35 b) t=0.75.
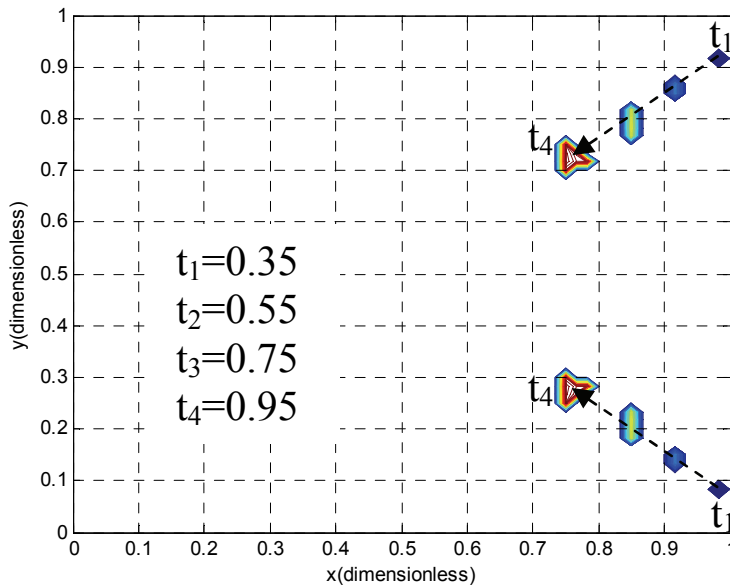
Figure 24: Peak point contours of σ_{xx} on 2D full Aluminum domain at several dimensionless times t=0.35, 0.55, 0.75, 0.95.
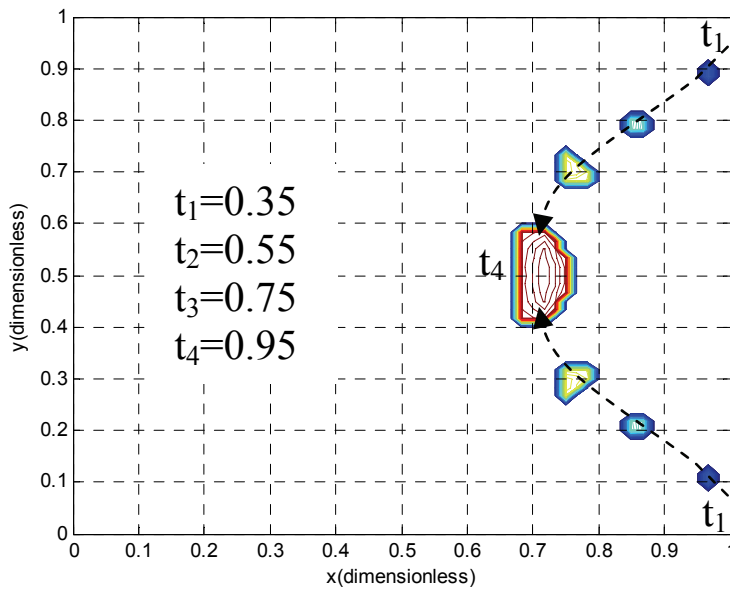
Figure 25: Peak point contours of σ_{xx} on 2D FG domain (p=1) at several dimensionless times t=0.35, 0.55, 0.75, 0.95.

in Figs. 26 and 27, the frequency of the displacement variation in the x-direction, u_x, is lower than the frequency of the displacement variation in the y-direction, u_y.

It may be observed from the figures that while the temperature field in the domains reaches the steady state after time t=10, the displacements or stresses continue to oscillate.
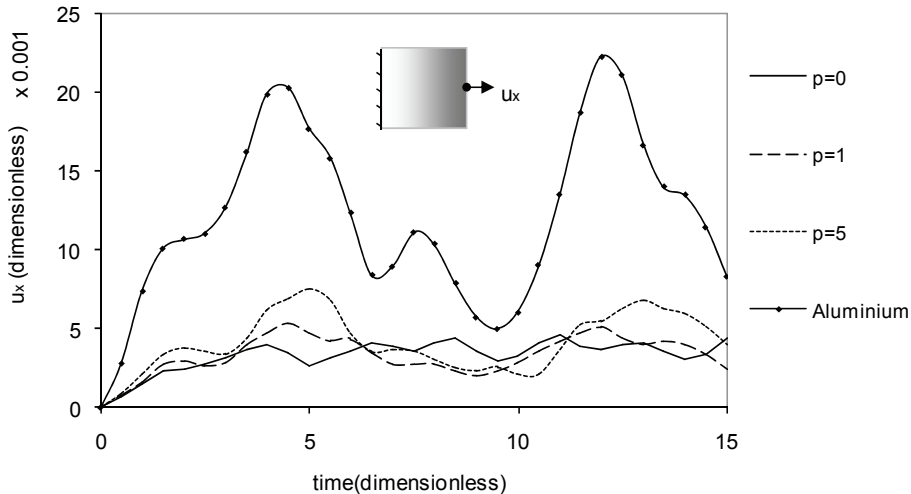
Figure 26: Variation of u_x at point (1,0.5) for various values of p.

In Fig. 28, the displacement wave front in the fully ceramic domain, p=0, is shown to propagate faster than the waves in the other domains while its amplitude is smaller. Thus, it can be concluded that by increasing the amount of Aluminum in the material, the wave speed will decrease due to the decreasing elastic modulus, while its amplitude will increase owing to increase in the coefficient of thermal expansion.

Fig. 29 shows the vertical displacements distribution on the top edge of the FG domain at dimensionless time t=1. High thermal diffusivity and thermal expansion of the FG domain with larger amount of Aluminum constituent (p=5) causes faster rise and larger displacement amplitudes compared to the other compositions (p<5). Even though in the FG domain (p=5) the volume fraction of Aluminum rapidly increases from the ceramic rich side to the metal rich side, including a very small amount of ceramic on the edge x=1 prevents vary large vertical displacements.

The rate of convergence for uniform node distribution is presented in Fig.30. In the convergence study the following error is introduced for normal stress, σ_x, over the
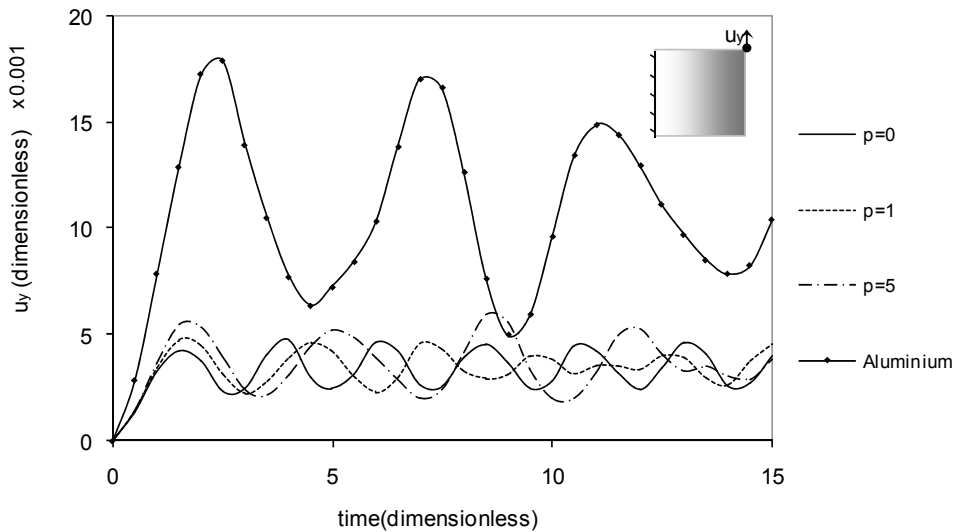
Figure 27: Variation of u_y at point (1,1) for various values of p.

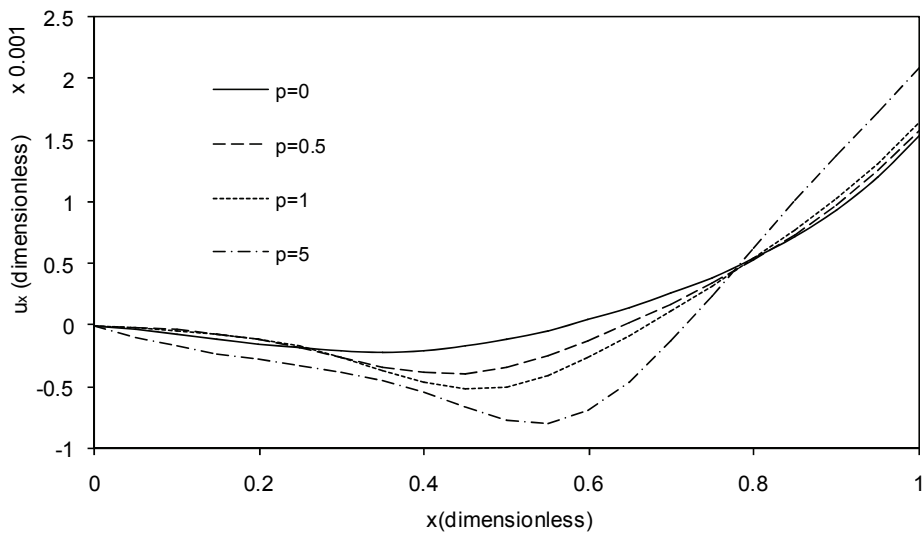Figure 28: displacement field along the x-direction on horizontal mid-line of 2D domains (y=0.5) at dimensionless time t=1
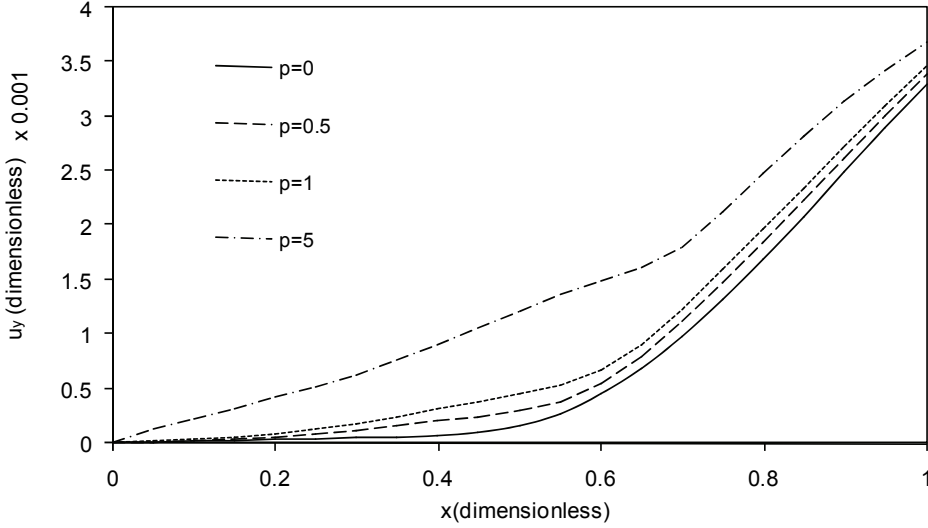
Figure 29: Displacement field along the y-direction on the top edge of the 2D domains (y=1) at dimensionless time t=1 for several values of *p*.

free boundary in right hand side:

$$Error = \int_0^{300\Delta\tau} \int_0^{l_y} \sigma_{xx}^2 \, dy \, dt \qquad (52)$$

In the free boundary in right hand side, exact normal stress is zero, so the error can be defined as Eq. 52. Errors are calculated for several numbers of nodes: $N_x = N_y = 7, 11, 21, 31$. According to this figure, the rate of convergence decreases by increasing the nodes.

The errors of normal stress in free boundary in right hand side, $x = l_x$, for two type of node distribution are obtained as stated by Eq. 52, the errors are compared in Fig.31. In concentrated node distribution, density of nodes near to the free boundary, $x = l_x$, is greater than other regions, but the number of nodes in concentrated distribution is same as in uniform distribution. Fig.31 shows that error in the free boundary decreases by increasing of node density around there, so that error in concentrated 21 by 21 nodes distribution is less than uniform 31 by 31 nodes distribution.

Influence of size of support domain on the error of normal stress for 21 by 21 node FG domain is shown in Fig.32. In this figure, $r = r_I^x = r_I^y$, $h = h_I^x = h_I^y$ and errors are obtained by Eq. 52. This figure shows that $r/h = 3$ introduce the minimum error.
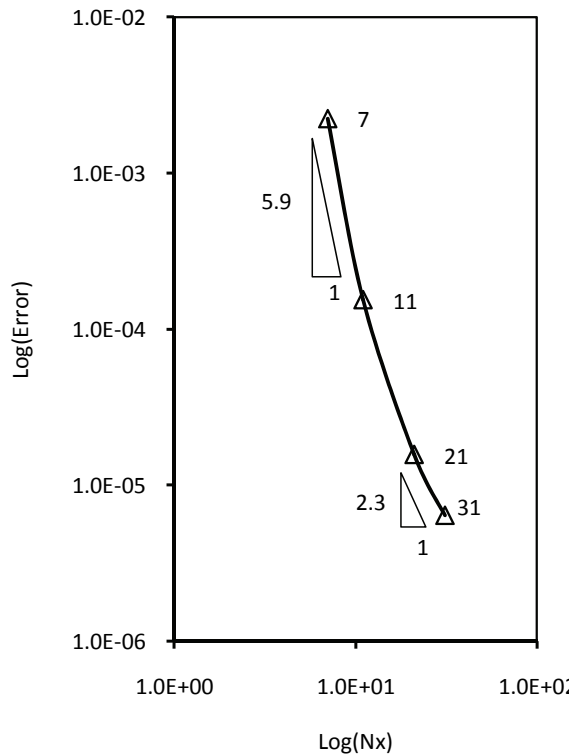
Figure 30: Rate of convergence of normal stress (error) over free boundary, $x = l_x$, for uniform node distribution in FG domain (p=1).

6   Conclusions

In this paper, two-dimensional thermo-elastic wave propagation in functionally graded (FG) materials under thermal loads was studied. To solve the nonlinear set of partial differential governing equations, the meshless local Petrov-Galerkin (MLPG) method was employed. By varying the volume fraction of the material constituents different material compositions have been achieved and the effect of the material composition on the thermo-elastic behavior of 2D FG domains was investigated.

The distribution and time evolution of temperature, displacements and stresses were presented and analyzed. The thermal field distribution throughout the geometry of the FG domain was obtained and the relevant longitudinal and transverse wave propagation were plotted.
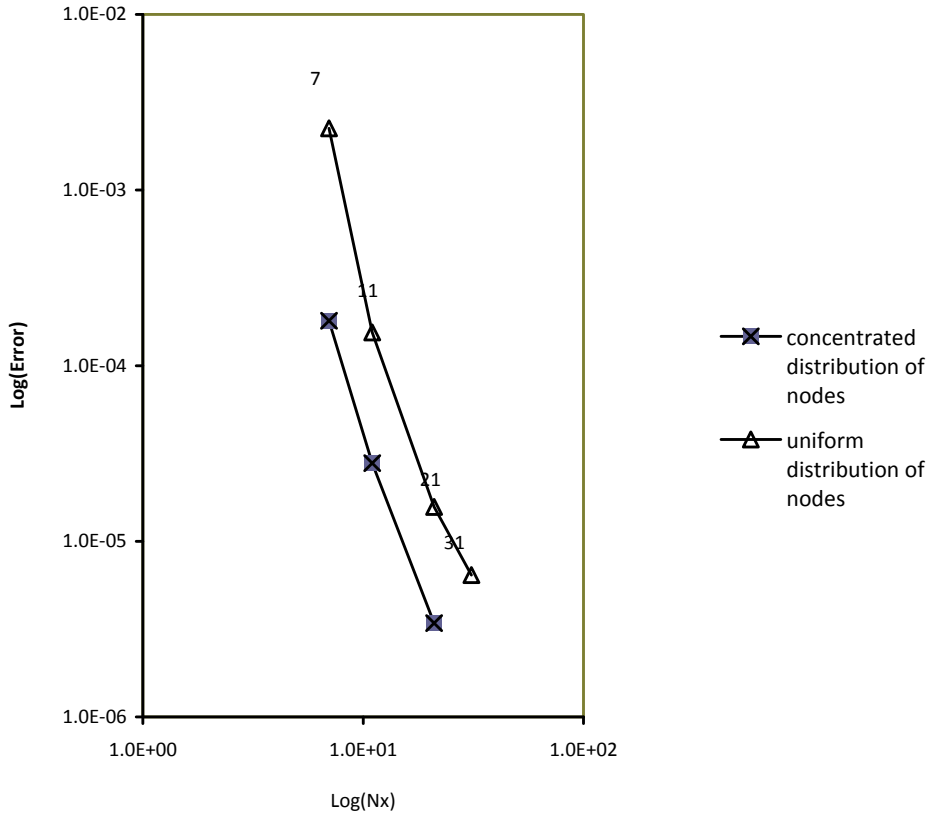
Figure 31: Compare of rate of error convergence in uniform node distribution and concentrated node distribution over free boundary, $x = l_x$, for FG domain (p=1).

The capability of the MLPG formulation to simulate the temperature distribution and predict thermal stresses in functionally graded materials was first verified before fully two-dimensional thermo-elasto-dynamic problems were solved. The main results of the analyses were:

- The wave propagation speed through a functionally graded material changes with position;

- The longitudinal wave speed is larger than the transverse wave speed;

- The wave speed is reduced from the ceramics rich side to the metal-rich side;

- While the speed of wave propagation decreases by increasing the amount of metal constituent, the temperature, displacement and stress amplitudes
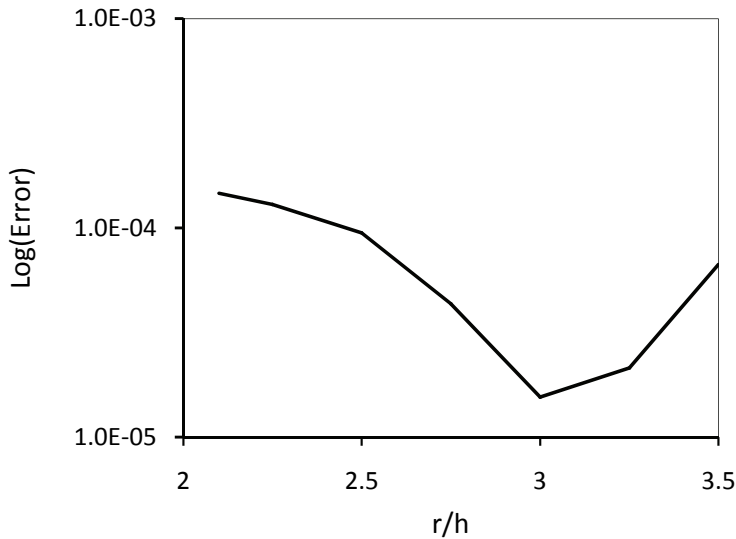
Figure 32: Influence of size of support domain on the normal stress (error) in the free boundary, $x = l_x$, for FG domain (p=1).

can increase, owing to more absorption of the energy into the domain and increased thermal expansion coefficients.

Based on these first results, future work includes:

- Simulation of cracked functionally graded materials;

- Inverse analysis for crack detection in functionally graded materials;

- Three-dimensional implementation and validation of the algorithm.

References

Atluri, S. N., Zhu, T. (1998): A new meshless local Petrov–Galerkin (MLPG) approach in computational mechanics. *Computational Mechanics,* Vol.22, pp. 117-127.

Atluri, S. N., Zhu, T. (1998): A new meshless local Petrov–Galerkin (MLPG) approach to nonlinear problems in computational modeling and simulation. *Comput. Modeling Simulation Eng.,* Vol. 3, pp. 187-196.

Atluri, S. N. (2004): *The Meshless Method (MLPG) for Domain & BIE Discretization,* Tech Science Press.

Atluri, S. N., Kim, H. G., Cho, J. Y. (1999): A critical assessment of the truly Meshless Local Petrov-Galerkin (MLPG), and Local boundary Integral Equation (LBIE) methods., *Computational Mechanics,* Vol. 24, pp. 348-372.

Belytschko, T., Black, T. (1999): Elastic crack growth in finite elements with minimal remeshing., *Int. J. Numer. Methods Eng.*, Vol. 45, pp. 601–620.

Belytschko, T., Lu, Y. Y., Gu, L. (1994): Element-free Galerkin methods. *Int. J. Numerical Methods in Engineering*, Vol. 37, pp. 229-256.

Berezovski, A., Engelbrecht, J., Maugin, G. A. (2003): Numerical simulation of two-dimensional wave propagation in functionally graded materials. *European Journal of Mechanics A/Solids*, Vol. 22, pp. 257-265.

Bordas, S., Rabczuk, T., Zi, G. (2008): Three-dimensional crack initiation, propagation, branching and junction in non-linear materials by extrinsic discontinuous enrichment of meshfree methods without asymptotic enrichment. *EFM*, Vol. 75, pp. 943-960.

Bordas, S. P. A.; Nguyen, P. V.; Dunant, C.; Dang, H. N.; Guidoum, A. (2006): An extended finite element library. *International Journal for Numerical Methods in Engineering*, Vol. 2, pp. 1-33.

Chi, L. F., Chung, Y. L. (2006): Mechanical behavior of functionally graded material plates under transverse load—Part I: Analysis., *Int. J. Solids and Structures,* Vol. 43, pp. 3657-3674.

Ching, H. K., Yen, S. C. (2005): Meshless local Petrov-Galerkin analysis for 2D functionally graded elastic solids under mechanical and thermal loads., *Composites: Part B Engineering*, Vol. 36, pp. 223-240.

Duarte, C. A., Oden, J. T. (1996): An h-p adaptive method using clouds. *Computer Methods in Applied Mechanics and Engineering*, Vol. 139, pp. 237-262.

Eslami, M. R., Babai, M. H., Poultangari, R. (2005): Thermal and mechanical stresses in a functionally graded thick sphere. *Int. J. Pressure Vessels and Piping,*

Vol. 82, pp. 522-527.

Eslami, M. R.; Akbari R. A.; Bagri, A.; Tajdari, M. (2007): Analysis of thermal stresses in two dimensional functionally graded domain using the meshless local Petrov-Galerkin method., *Taiwan s.n., Seventh Int. Cong. Thermal stresses.*

Fries, T. P., Matthies, H. G. (2003): *Classification and overview of meshfree methods.* Technische Universität Braunschweig. Braunschweig: Informatikbericht-Nr.

Han, X., Liu, G. R., Xi, Z. C., Lam, K. Y. (2001): Transient waves in a functionally graded cylinder. *Int. J. solids and structures,* Vol. 38, pp. 3021-3037.

Hasselman, D. P. H., Youngblood, G. E. (1978): Enhanced thermal stress resistance of structural ceramics with thermal conductivity gradient. *Journal of the American Ceramic Society,* Vol. 61, pp. 49-52.

Hatta, H., Taya, M. (1985): Effective thermal conductivity of a misoriented short fiber composite. *Applied Physics,* Vol. 58, pp. 2478-2486.

Heaney, C., Augarde, C., Deeks, A. (2010): Modelling Elasto-Plasticity Using the Hybrid MLPGMethod, *CMES: Computer Modeling in Engineering & Sciences* Vol. 56, pp. 153-176.

Hetnarski, R. B., Eslami, M. R. (2008): *Thermal stresses, Advanced Theory and Applications.* Netherland : Springer.

Houbolt, J. C. (1950): A recurrence matrix solution for the dynamic response of elastic aircraft. *J. of Aeronautical Sciences*, Vol. 17, pp. 371-376.

Huerta, A., Belytschko, T., Fernandez-Mendez, S., Rabczuk, T. (2004): *Encyclopedia of Computational Mechanics,* chapter Meshfree Methods. s.l.: John Wiley and Sons.

Karihaloo, B. L., Xiao, Q. Z. (2003): Modelling of stationary and growing cracks in FE framework without remeshing: a state-of-the art review. *Computers and Structures*, Vol. 81, pp. 119-129.

Kim, H. G., Atluri, S. N. (2000): Arbitrary Placement of Secondary Nodes, and Error Control, in the Meshless Local Petrov-Galerkin (MLPG) Method., *CMES: Computer Modeling in Engineering & Sciences*, Vol. 1, pp. 11-32.

Liu, G. R., Han, X., Lam, K. Y. (1999): Stress waves in functionally gradient materials and its use for material Characterization. *Composites: Part B Engineering,* Vol. 30, pp. 383-394.

Liu, W. K., et al. (1996): Advances in multiple scale kernel particle methods. *Computational Mechanics,* Vol. 18, pp. 73-111.

Melenk, J.M., Babuska, I. (1996): The partition of unity finite element method: basic theory and applications., *Comput. Meth. Appl. Mech. Engrg,* Vol. 139, pp.

1-4.

Mori, T and Tanaka, K. (1973): Average stress in matrix and average elastic energy of materials with misfitting inclusions. *Acta Metallurgica*, Vol. 21, pp. 571-574.

Nayroles, B., Touzot, G., Villon, P. (1992): Generalizing the finite element method diffuse approximation and diffuse elements. *Computational Mechanics,* Vol. 10, pp. 307-318.

Nguyen, V. P., Rabczuk, T., Bordas, S., Duflot, M. (2008): Meshless methods: A review and computer implementation aspects. *Mathematics and Computers in Simulation*, Vol. 79, pp. 763-813.

Noda, N., Tsuji, T. (1990): Steady thermal stresses in a plate of a functionally gradient material. Sendai, Japan: s.n., Proc. *1st Int. Symp. on functionally gradient materials*. pp. 339-344.

Qian, L. F., Batra, R. C. (2004): Transient thermoelastic deformations of a thick functionally graded plate., *Journal of Thermal Stresses,* Vol. 27, pp. 705-740.

Qian, L. F., Batra, R. C. (2005): Three-dimensional transient heat conduction in a functionally graded thick plate with a higher-order plate theory and a meshless local Petrov-Galerkin method. *Computational Mechanics*, Vol. 35, pp. 214-226.

Qian, L. F., Ching, H. K. (2004): Static and dynamic analysis of 2-D functionally graded elasticity by using meshless local Petrov-Galerkin method, *Journal of the Chinese Institute of Engineers,* Vol. 27, pp. 491-503.

Rabczuk, T., Bordas, S., Zi, G. (2007): A three-dimensional meshfree method for continuous crack initiation, nucleation and propagation in statics and dynamics., *Computational Mechanics*, Vol. 40, pp. 473-495.

Rabczuk, T., Bordas, S., Nguyen, P. V., Zi, G. (2008): A geometrically non-linear three-dimensional cohesive crack method for reinforced concrete structures. *EFM*, Vol. 75, pp. 4740-4758.

Reddy, J. N., Wang, C. M., Kitipornchai, S. (1999): Axisymmetric bending of functionally graded circular and annular plates. *European Journal of Mechanics A/Solids*, Vol. 18, pp. 185-199.

Rosen, B. W., Hashin, Z. (1970): Effective thermal expansion coefficients and specific heats of composite materials. *International Journal of Engineering Science,* Vol. 8, pp. 157-173.

Shakeri, M., Akhlaghi, M., Hoseini, S. M. (2006): Vibration and radial wave propagation velocity in functionally graded thick hollow cylinder. *Composite Structures*, Vol. 76, pp. 174-181.

Sladek, J., Sladek, V., Solek, P. (2009): Elastic analysis in 3D anisotropic func-

tionally graded solids by the MLPG, *CMES: Computer Modeling in Engineering & Sciences,* Vol. 43, pp. 223-251.

Sladek J., Sladek, V.; Solek, P.; Wen, P. H.; Atluri, S. N. (2008): Thermal analysis of Reissner-Mindlin shallow shells with FGM properties by the MLPG, *CMES: Computer Modeling in Engineering & Sciences* Vol. 30, pp. 77-97.

Sladek, J., Sladek, V., Hon, Y. C. (2006): Inverse heat conduction problems by meshless local Petrov–Galerkin method. *Engineering Analysis with Boundary Elements,* Vol. 30, pp. 650-661.

Sladek, J., Sladek, V., Tan, C. L., Atluri, S. N. (2008): Analysis of transient heat conduction in 3D anisotropic functionally graded solids by the MLPG, *CMES: Computer Modeling in Engineering & Sciences,* Vol. 32, pp. 161-174.

Sladek, J., Sladek, V., Wünsch, M., Zhang, Ch. (2009): Interface Crack Problems in Anisotropic Solids Analyzed by the MLPG, *CMES: Computer Modeling in Engineering & Sciences,* Vol. 54, pp. 223-252.

Sladek, J., Sladek, V., Zhang, Ch., Solek, P. (2007): Application of the MLPG to Thermo-Piezoelectricity, *CMES: Computer Modeling in Engineering & Sciences* Vol. 22, pp. 217-233.

Sladek, J., Sladek, V., Solek, P., Tan, C. L., Zhang, Ch. (2009): Two- and three-dimensional transient thermoelastic analysis by the MLPG method, *CMES: Computer Modeling in Engineering & Sciences,* Vol. 47, pp. 61-95.

XueHong, W. U., Shen, S. P., Tao, W. Q. (2007): Meshless Local Petrov-Galerkin Collocation Method for Two-dimensional Heat Conduction Problems, *CMES: Computer Modeling in Engineering & Sciences*, Vol. 22, pp.65-76.

Zhang, G. M., Batra, R. C. (2007): Wave propagation in functionally graded materials by modified smoothed particle hydrodynamics (MSPH) method. *J. computational physics*, Vol. 222, pp. 374-390.